

**Climates of the last three interglacials in subtropical eastern Australia inferred from wetland sediment geochemistry**

Author

Kemp, CW, Tibby, J, Arnold, LJ, Barr, C, Gadd, PS, Marshall, JC, McGregor, GB, Jacobsen, GE

Published

2020

Journal Title

Palaeogeography, Palaeoclimatology, Palaeoecology

Version

Accepted Manuscript (AM)

DOI

[10.1016/j.palaeo.2019.109463](https://doi.org/10.1016/j.palaeo.2019.109463)

Rights statement

© 2020 Elsevier. Licensed under the Creative Commons Attribution-NonCommercial-NoDerivatives 4.0 International Licence (<http://creativecommons.org/licenses/by-nc-nd/4.0/>) which permits unrestricted, non-commercial use, distribution and reproduction in any medium, providing that the work is properly cited.

Downloaded from

<http://hdl.handle.net/10072/394624>

Griffith Research Online

<https://research-repository.griffith.edu.au>

## **Climates of the last three interglacials in subtropical eastern Australia inferred from wetland sediment geochemistry**

Kemp, C.W.<sup>1</sup>, Tibby, J.<sup>1</sup>, Arnold, L.J.<sup>2</sup>, Barr, C.<sup>1</sup>, Gadd, P.S.<sup>3</sup>, Marshall, J.C.<sup>4,5</sup>, McGregor, G.B.<sup>4</sup>, Jacobsen, G.E.<sup>3</sup>

1. Geography, Environment and Population and Sprigg Geobiology Centre, University of Adelaide, North Terrace Campus, Adelaide, 5005, SA, Australia
2. School of Physical Science, Environment Institute, Sprigg Geobiology Centre and Institute for Photonics and Advanced Sensing, University of Adelaide, North Terrace Campus, Adelaide, 5005, SA, Australia
3. Australian Nuclear Science and Technology Organisation, Locked Bag 2001, Kirrawee DC, New South Wales 2232, Australia
4. Queensland Department of Environment and Science, Dutton Park, Queensland, Australia
5. Australian Rivers Institute, Griffith University, Nathan, 4111, Queensland, Australia

### **Corresponding author details:**

Christopher Kemp

**Email:** [Christopher.kemp@adelaide.edu.au](mailto:Christopher.kemp@adelaide.edu.au)

**Postal address:** Department of Geography, Environment and Population, The University of Adelaide, North Terrace, Adelaide, South Australia, 5005

## Abstract

Records of Australian climate during Marine Isotope Stages 5 and 7 (130–71 and 243–191 ka) are rare, preventing detailed assessments of long-term climate, drivers and ecological responses across the continent over glacial-interglacial timescales. This study presents a geochemistry-based palaeoclimate record from Fern Gully Lagoon on North Stradbroke Island (also known as Minjerribah) in subtropical eastern Australia, which records climates in MIS 7a–c, MIS 5 and much of the Holocene, in addition to MIS 4 (71–57 ka), and parts of MIS 6, MIS 3 and MIS 2 (191–130, 57–29 and 29–14 ka). Indicators of inorganic sedimentation from a 9.5 m sediment core – focussed on high-resolution estimates of sediment geochemistry supported by x-radiography, inorganic content and magnetic susceptibility – were combined with a chronology consisting of six radiocarbon ( $^{14}\text{C}$ ) and thirteen single-grain optically stimulated luminescence (OSL) ages. Hiatuses occurred at ~178–153 ka, ~36–21 ka and ~7–2 ka and likely result from the wetland drying. Low values of locally sourced aeolian materials indicate a wet MIS 7a–c and early MIS 6 before a relatively dry MIS 5. Inorganic flux during the Holocene was up to four times greater than during MIS 5, consistent with long-term interglacial drying observed in other regions, most notably in central Australia. This study highlights the importance of employing a combination of multiple dating approaches and calibrated geochemical proxies to derive climate reconstructions and to identify depositional complexities in organic-rich wetland records.

**Key words:** Palaeoclimate, North Stradbroke Island, Holocene, MIS 5, MIS 7,  $\mu\text{XRF}$

## 1. Introduction

Reliable reconstructions of past interglacial climates are important for providing analogues of future climate change, as well as for better understanding ecosystem responses that are likely to accompany increases in global temperature (Turney and Jones, 2010; Harrison and Bartlein, 2012). Records of interglacial climates are similarly required to understand the long-term evolution of Australian biota including past extinction events (Kershaw et al., 2003; Miller et al., 2016; van der Kaars et al., 2017). At present, the usefulness of Australian palaeoclimate records for either of these purposes is relatively limited, as most only extend to the Last Glacial Maximum (LGM) ~20 thousand years ago (ka) (Petherick et al., 2013; Reeves et al., 2013).

Records of Australian climate during the past three interglacials are limited, but include Lynch's Crater and the nearby ODP 820 marine record (Kershaw et al., 2007a; Moss and Kershaw, 2007) in the north-east; Lake Eyre, Lake Woods and central Australian streams and lakes (Bowler et al., 1998; Nanson et al., 2008; Cohen et al., 2015; Fu et al., 2017); and the Naracoorte Caves, Lake Selina, Lake Wangoom and Caledonia Fen in the south-east (Ayliffe et al., 1998; Colhoun et al., 1999; Harle et al., 2002; Kershaw et al., 2007b). The distribution of available records is limited in geographical scope, and does not currently include equatorial or subtropical Australian localities. Additionally, while these records infer past climate from proxies such as pollen, charcoal and palaeoshorelines, there is not as yet an Australian interglacial record utilising  $\mu$ XRF geochemical analysis.

Climate records derived from geochemical studies of wetland sediments have experienced a boom in the past decade, with the advent of relatively cheap, reliable, reproducible  $\mu$ XRF analysis (Croudace and Rothwell, 2015). Wetland geochemical records represent invaluable archives for palaeoclimatology reconstructions, providing constraints on climate change at local (e.g. Eggenberger et

al., 2018; Vegas-Vilarrúbia et al., 2018; Burrows et al., 2016) and regional scales (e.g. Field et al., 2018; Pleskot et al., 2018; Profe et al., 2018), and enabling a greater understanding of internal wetland processes (e.g. Burrows et al., 2016; Kienel et al., 2017; Vegas-Vilarrúbia et al., 2018).

Here we present a multi-proxy ~209 kyr record of subtropical climatic variability from Fern Gully Lagoon focussing on past interglacials. This study is the foundation for future studies of regional climate change based on Fern Gully Lagoon sediments and assesses the validity of the site as a palaeoclimate archive. We use calibrated  $\mu$ XRF Itrax scanning to infer locally-derived aeolian inorganic sedimentation and assess the suitability of OSL and  $^{14}\text{C}$  to date the complex, organic-rich sediment sequence.

## **2. Background**

### **2.1 Global climate changes during recent interglacials**

A recent review of global interglacial climates has demonstrated some important differences between marine isotope stage 7 (MIS 7), MIS 5 and the Holocene (Berger et al., 2015). Specifically, the MIS 7 interglacial complex was characterised by higher average global temperatures than the MIS 5 interglacial complex but had a lower temperature peak in MIS 7e than that in MIS 5e (Lisiecki and Raymo, 2005; Parrenin et al., 2013; Berger et al., 2015). The lower MIS 7e temperature is likely due to the greater difference between MIS 5e summer and winter insolation, while insolation during MIS 7e was more evenly distributed over the seasons due to lower obliquity of the Earth's orbit (Berger et al., 2015). In contrast to the warmer MIS 5e, the warmer climates of the MIS 7a–c sub-complex relative to the MIS 5a–c sub-complex are reflected in extended periods of reduced ice volume (Lisiecki and Raymo, 2005; Elderfield et al., 2012), higher sea levels (Rohling et al., 2009) and higher atmospheric  $\text{CO}_2$  concentrations (Köhler et al., 2017). MIS 7a–c represents a rare ~20 kyr period of relatively stable, warm, mean global climate (Berger et al., 2015).

Sea surface temperature records from the West Pacific Warm Pool (WPWP) can be used to guide understanding of globally-linked, regional changes in eastern Australian climate that occurred during the previous three interglacials (Zhang et al., 2017). In particular, sea surface temperatures in the WPWP (Fig. 1) can dictate climate variability in the wider region, including the central-eastern Australian coast and the Tasman Sea (Martinez et al., 2002; Bostock et al., 2006; Pelejero et al., 2006). WPWP sea surface temperatures indicate that MIS 5e had the warmest SSTs of the last ~250 kyr (Tachikawa et al., 2014), but that the MIS 7 interglacial complex and the Holocene were/are warmer than the MIS 5 interglacial complex by an average of  $\sim 1 - 2^{\circ}\text{C}$  (Lo et al., 2017).

## **2.2 Australian climates during past interglacials**

The available Australian MIS 7 data permits insights into broad-scale climatic trends. During late MIS 7, Lakes Eyre and Woods in central Australia, which are predominantly fed by monsoonal rains, were full, in contrast to their present mostly dry state (Bowler et al., 1998; Fu et al., 2017). Meanwhile, wet climates and open water were present in Lynch's Crater in ENSO-dominated north-eastern Australia (Kershaw et al., 2007a; Moss and Kershaw, 2007). Similarly, the speleothem record from the Naracoorte Caves in south-eastern Australia, which primarily reflects southern westerly wind-dominated rainfall, indicates wet climates, with pronounced periods of calcitic growth between  $\sim 220$  and 155 ka (Ayliffe et al., 1998). These few available records indicate that Australia was wetter during late MIS 7 than the Holocene, with a more active Australian Monsoon in the north and stronger or more northerly southern westerly winds.

Central Australia was also wet during MIS 5 (Bowler et al., 1998; Cohen et al., 2015), though the average precipitation:evaporation ratio was lower than during late MIS 7. North-eastern Australian records indicate wet climates during MIS 5, but greater climate variability than during MIS 7 (Kershaw et

al., 2007a; Moss and Kershaw, 2007). The pattern in the south-east of the continent is in general agreement with north-eastern records, with generally wet climates observed during MIS 5 (Edney et al., 1990; Ayliffe et al., 1998; Colhoun et al., 1999; Harle et al., 2002).

Holocene hydroclimate in Australia was drier than MIS 5 and MIS 7 in most regions. Lake Eyre and Lake Frome, which were full during MIS 5, became dry and ephemeral (Cohen et al., 2015), while speleothem growth largely ceased in the Naracoorte Caves (Ayliffe et al., 1998) suggesting weakening or more southerly south westerly winds. However, there is uncertainty about whether the Holocene was drier than MIS 5 in south-east Australia and the Wet Tropics of north-eastern Australia within each record (Edney et al., 1990; Colhoun et al., 1999; Kershaw et al., 2007a; Kershaw et al., 2007b). Uncertainty within records combined with geographical separation makes it difficult to determine climate change at a continental scale. As such, additional records from new locations are required.

### **2.3 Study site**

North Stradbroke Island is a sand island located along the eastern coast of Australia (Fig. 1). The Island is part of the world's oldest and largest coastal dune system (Patton et al., 2019) and lies on an aeolian dust pathway from central and south-central Australia (McGowan et al., 2008; Petherick et al., 2009). The Island is a strategic location for understanding palaeoclimate, as it is situated in the subtropics (Fig. 1), with a contemporary climate that is strongly influenced by the El Niño – Southern Oscillation (ENSO) (Barr et al., 2019) and preserves the highest density of wetlands with sediment dating to the LGM in Australia (Tibby et al., 2017). As such, it has been the focus of several detailed palaeoenvironmental reconstructions (e.g. Moss et al., 2013; Barr et al., 2017; Petherick et al., 2017; Cadd et al., 2018), the longest of which extends to ~130 ka (Cadd et al., 2018). There is evidence for

human occupation of the island from at least 20 ka at Wallen Wallen Creek (Fig. 1), with a Holocene increase in human occupation peaking at ~1 ka (Neal and Stock, 1986).

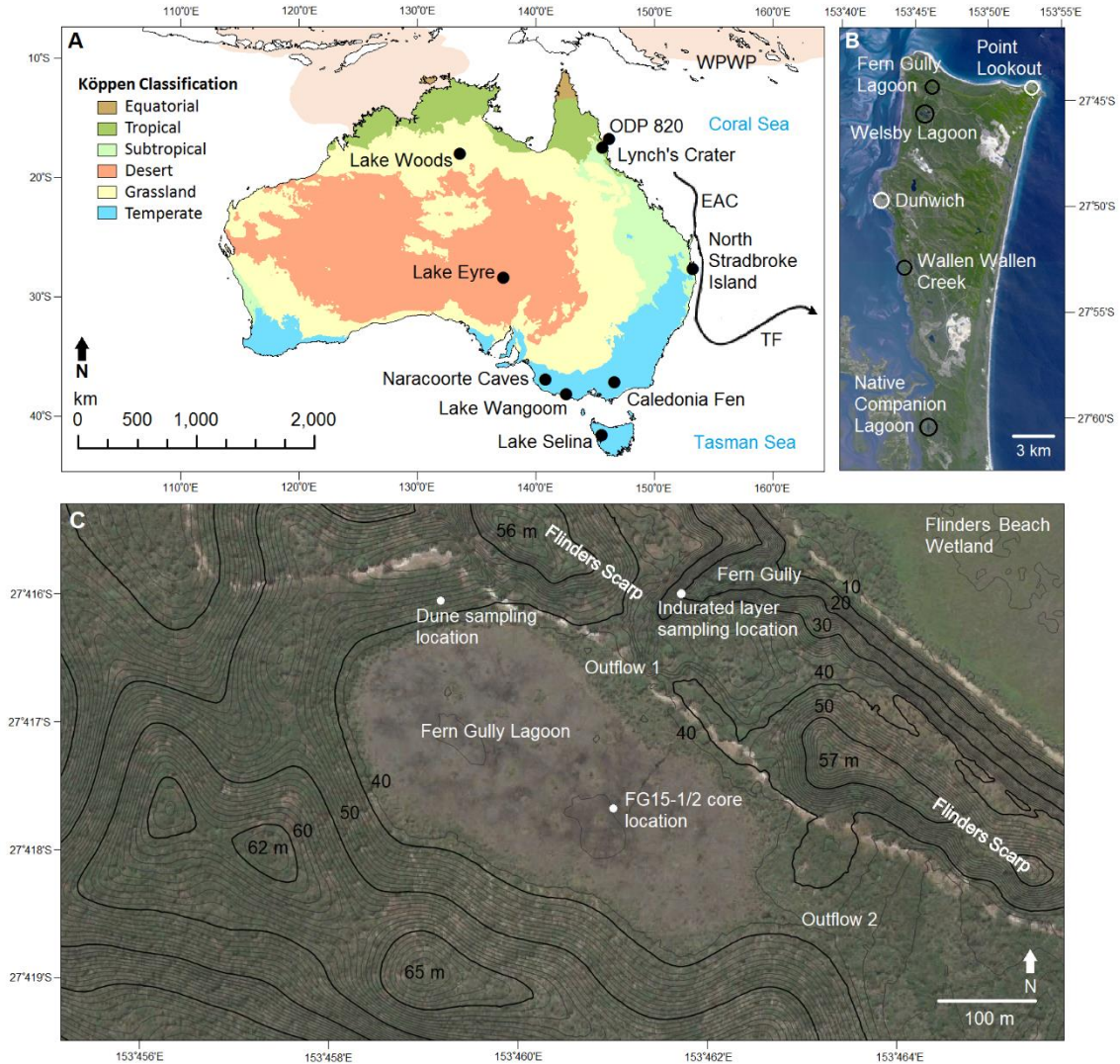


**Figure 1:** **A:** Modified Köppen climate zones (BOM, 2005), location of Australian interglacial climate records and the approximate current positions of the west Pacific warm pool (WPWP, mean annual SST >28°C) boundary (pink shading; (Gagan et al., 2000)), the East Australian Current (EAC) and the Tasman Front (TF) (Bostock et al., 2006). **B:** North Stradbroke Island, with the four climate/archaeological record sites (black circles) and local towns (white circles), mentioned in the text. **C:** Fern Gully Lagoon combined topographic map and satellite image, indicating the coring location, locations of modern geochemistry samples, outflows and the height of surrounding dunes (m ASL).

Fern Gully Lagoon (27.417°S, 153.460°E, 39 m ASL) is an approximately 0.8 km<sup>2</sup> perched, palustrine wetland (Leach, 2011) that lies within a shallow bowl of vegetated dunes at the north-western end of North Stradbroke Island. The wetland has two above-ground outflows, the largest being to the eponymous Fern Gully (Fig. 1c). The limited catchment area and highly permeable sandy soils mean the delivery of fluviially transported material to the wetland is limited. Single-grain OSL dating of a reconnaissance core from Fern Gully Lagoon determined a preliminary basal age of  $\sim 208.4 \pm 32.5$  ka (Tibby et al., 2017) at a depth of 9.25 meters.

### **3. Methods**

#### **3.1 Core collection and correlation**

In 2015, two  $\sim 9$  m-long cores were extracted from the approximate centre of Fern Gully Lagoon (27.4174°S, 153.4600°E) using a modified Bolivia corer, itself a modification of the Livingstone-square-rod piston-sampling method (Wright, 1967). The two cores were offset by one metre horizontally and 50 cm vertically, in an attempt to provide a continuous sequence. Cores were extracted in black-painted PVC pipe and stored in black plastic sleeves, to eliminate light contamination and ensure the sediments would be suitable for luminescence dating. The first core (FG15-1) was chosen as the master core and was sampled for single-grain OSL and <sup>14</sup>C dating. The second core (FG15-2) was used to fill gaps in the FG15-1 record and to provide additional sediment for <sup>14</sup>C and conventional wave dispersive x-ray fluorescence analyses.

Cores were aligned using CPLSlot sequence slotting software (Clark and Hounslow, 2009) using the eight elements with highest Itrax counts per second: silicon, titanium, zircon, potassium, calcium, iron and bromine. The correlation allowed the cores to be placed on a common depth scale.

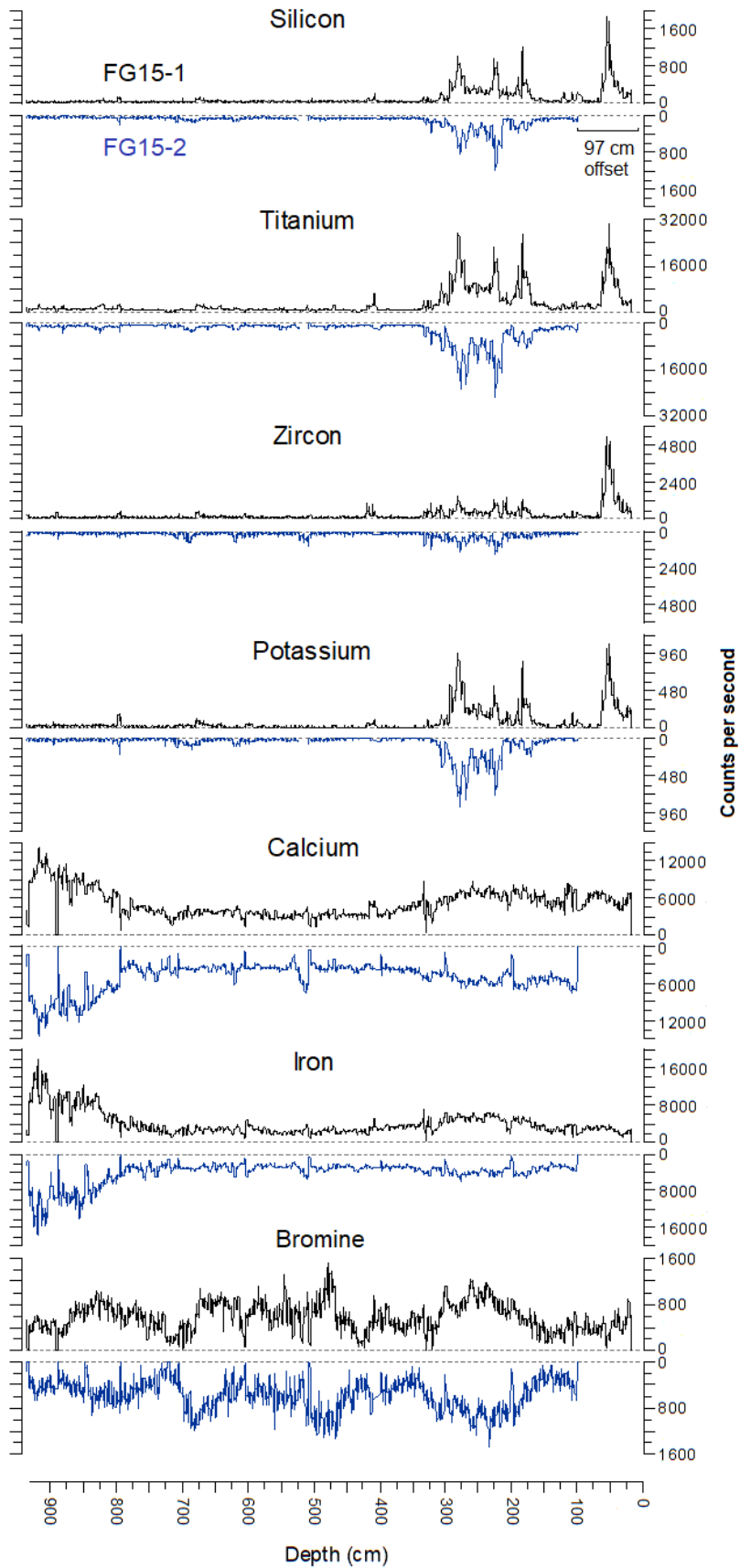


**Figure 2:** Relative position of FG15-2 to FG15-1 using the seven elements exhibiting the highest counts per second.

Moisture and organic content were determined on 930 one cubic centimetre samples following Heiri et al. (2001). This record was used to target optimum OSL sample locations (i.e., locate areas with highest inorganic content, and presumably quartz content) and to calculate average water content and sediment densities for luminescence dose rate calculation (See supplementary materials).

### **3.2 Itrax $\mu$ XRF, magnetic susceptibility and X-radiography**

To determine changes in sediment geochemistry, Itrax second-generation micro X-ray fluorescence ( $\mu$ XRF, Croudace et al., 2006) scanning of both cores was undertaken at the Australian Nuclear Science and Technology Organisation. Itrax scanning utilised a molybdenum x-ray tube at 30 kV and 55 mA, with a 20 second exposure time, generating a record of elemental response (counts per second) for thirty-five elements at 2 mm intervals. An X-radiograph record using the same tube at 45 kV at 30 mA and a magnetic susceptibility record were also developed.

Micro XRF data must be normalised to mitigate the closed-sum effect (Weltje and Tjallingii, 2008; Löwemark et al., 2011). However, despite an increasing number of  $\mu$ XRF studies (Croudace and Rothwell, 2015), there is no standardised method for normalisation. To identify all recently published methods, we undertook a review and synthesis of  $\mu$ XRF in the Scopus (<https://www.scopus.com/home.uri>) and Web of Science (<http://www.webofknowledge.com>) databases. The results of this review were used to identify which normalisation methods have been utilised in recent  $\mu$ XRF studies, along with what (if any) validation and calibration methods were used (e.g. conventional XRF, inductively coupled plasma mass spectrometry (ICP-MS)). Further details of the database review methods and results, along with a discussion of recent  $\mu$ XRF methodologies are provided in the supplementary material.

The eight most common normalisation methods identified in our review were assessed to determine the best method for normalising the Fern Gully Lagoon  $\mu$ XRF record. These were: total

counts per second normalisation (Bouchard et al., 2011; Martin et al., 2014), centred log-ratio normalisation (Weltje and Tjallingii, 2008; Weltje et al., 2015), aluminium normalisation (Brumsack, 2006; Löwemark et al., 2011), titanium normalisation (Vegas-Vilarrúbia et al., 2018), silicon normalisation, zircon normalisation, normalisation using incoherent scattering (Compton scattering) and the ratio of incoherent to coherent scattering (Rayleigh and Compton scattering) (e.g. Guyard et al., 2007; Kylander et al., 2011; Marshall et al., 2011; Berntsson et al., 2014).

The normalised  $\mu$ XRF data were compared to quantitative conventional XRF analyses at twenty locations from core FG15-2, following a similar method to recent studies (e.g. Hahn et al., 2014; Falster et al., 2018; Profe et al., 2018). The conventional XRF sample locations were chosen to represent the broadest range of  $\mu$ XRF-derived concentrations, but where there was little within-sample variability in  $\mu$ XRF readings. The latter consideration was important since due to the high sediment organic content, it was necessary to sample up to 1 cm of the core to ensure sufficient material for XRF. Conventional XRF analysis was undertaken at the Commonwealth Scientific and Industrial Research Organisation in Adelaide, South Australia, using lithium-borate fusion of sample material. The glass discs created from the fusion procedure were subsequently analysed on a PANalytical Axios Advanced wavelength dispersive XRF (WD-XRF) system using an in-house silicates calibration program.

For normalisation methods without internal XRF calibration (all but centred log-ratio),  $\mu$ XRF counts per second were compared to absolute concentrations using simple linear regressions. The normalisation method with the highest coefficient of variation was used to identify the most suitable normalisation method for Fern Gully Lagoon sediments. For centred log-ratio, we used a Matlab script after Grant et al. (2017) to produce a multivariate centred log-ratio corrected dataset. This XRF calibration was then used to calculate the approximate mass of oxides for the composite record.

The commonly utilised  $\mu$ XRF incoherent/coherent scattering ratio was also evaluated as a qualitative indicator of sediment organic content (e.g. Guyard et al., 2007; Jouve et al., 2013; Field et al., 2018; Woodward et al., 2018).  $\mu$ XRF water content corrections were also calculated after Boyle et al. (2015), as the sediments have a high water content that is likely to affect  $\mu$ XRF readings.

### **3.3 Identification of the aeolian component in the Fern Gully Lagoon $\mu$ XRF record**

McGowan et al. (2008) demonstrated that the inorganic component of wetland sediments on North Stradbroke Island (NSI) is derived from two main sources; the local silicon-rich and trace element-depleted sands, and far-travelled dust, which is more clay-rich. Petherick et al. (2009) expanded on that study, analysing source material from 149 sites in central and eastern Australia to geochemically fingerprint far-travelled dust deposited in Native Companion Lagoon (Fig. 1b). High quantities of scandium, gallium, thallium and nickel characterise the clay-rich, far-travelled sediment, contrasting with the Island's rare earth element-depleted silicon-rich quartz sands (McGowan et al., 2008; Petherick et al., 2009). While scandium, gallium and nickel were identified in the  $\mu$ XRF scan, their concentration was too low to be accurate, and they were not considered further.

We derived a high-resolution record of calibrated  $\mu$ XRF silicon. Higher silicon input into wetlands is indicative of drier climate on NSI, which reduces protective vegetation cover (McGowan et al., 2008; Petherick et al., 2009). This effect is amplified by the sandy soils of NSI, which are generally loose and very dry due to their high permeability (Leach, 2011), which also restricts overland flow.

Element	Material quantified by XRF	Total cts/s normalised	Centered log ratio	Raw cts/s	Al normalised	Total scatter normalised	Incoherent scatter normalised
Zircon (Zr)	pure element (ppm)	$r^2 = 0.93, p < 0.05$	$r^2 = 0.65, p < 0.05$	$r^2 = 0.92, p < 0.05$	$r^2 = 0.83, p < 0.05$	$r^2 = 0.92, p < 0.05$	$r^2 = 0.92, p < 0.05$
Titanium (Ti)	TiO <sub>2</sub>	$r^2 = 0.88, p < 0.05$	$r^2 = 0.66, p < 0.05$	$r^2 = 0.90, p < 0.05$	$r^2 = 0.80, p < 0.05$	$r^2 = 0.90, p < 0.05$	$r^2 = 0.89, p < 0.05$
Potassium (K)	K <sub>2</sub> O	$r^2 = 0.83, p < 0.05$	$r^2 = 0.79, p < 0.05$	$r^2 = 0.85, p < 0.05$	$r^2 = 0.73, p < 0.05$	$r^2 = 0.85, p < 0.05$	$r^2 = 0.84, p < 0.05$
Silicon (Si)	SiO <sub>2</sub>	$r^2 = 0.80, p < 0.05$	$r^2 = 0.57, p < 0.05$	$r^2 = 0.78, p < 0.05$	$r^2 = 0.65, p < 0.05$	$r^2 = 0.77, p < 0.05$	$r^2 = 0.76, p < 0.05$
Bromine (Br)	pure element (ppm)	$r^2 = 0.71, p < 0.05$	$r^2 = 0.84, p < 0.05$	$r^2 = 0.44, p < 0.05$	$r^2 = 0.61, p < 0.05$	$r^2 = 0.44, p < 0.05$	$r^2 = 0.42, p < 0.05$
Calcium (Ca)	CaO	$r^2 = 0.74, p < 0.05$	$r^2 = 0.78, p < 0.05$	$r^2 = 0.42, p < 0.05$	$r^2 = 0.54, p < 0.05$	$r^2 = 0.42, p < 0.05$	$r^2 = 0.43, p < 0.05$
Sulfur (S)	SO <sub>3</sub>	$r^2 = 0.73, p < 0.05$	$r^2 = 0.70, p < 0.05$	$r^2 = 0.30, p < 0.05$	$r^2 = 0.33, p < 0.05$	$r^2 = 0.28, p < 0.05$	$r^2 = 0.26, p < 0.05$
Iron (Fe)	Fe <sub>2</sub> O <sub>3</sub>	$r^2 = 0.53, p < 0.05$	$r^2 = 0.55, p < 0.05$	$r^2 = 0.50, p < 0.05$	$r^2 = 0.44, p < 0.05$	$r^2 = 0.50, p < 0.05$	$r^2 = 0.49, p < 0.05$
Gallium (Ga)	pure element (ppm)	$r^2 = 0.11, p = 0.16$	$r^2 = 0.19, p = 0.05$	$r^2 = 0.03, p = 0.48$	$r^2 = 0.20, p < 0.05$	$r^2 = 0.01, p = 0.69$	$r^2 = 0.01, p = 0.72$
Aluminum (Al)	Al <sub>2</sub> O <sub>3</sub>	$r^2 = 0.09, p = 0.19$	$r^2 = 0.09, p = 0.19$	$r^2 = 0.62, p < 0.05$	N/A	$r^2 = 0.67, p < 0.05$	$r^2 = 0.69, p < 0.05$
Magnesium (Mg)	MgO	$r^2 = 0.05, p = 0.33$	$r^2 = 0.85, p < 0.05$	$r^2 < 0.01, p = 0.79$	$r^2 = 0.08, p = 0.22$	$r^2 = 0.02, p = 0.60$	$r^2 = 0.02, p = 0.55$
Phosphorus (P)	P <sub>2</sub> O <sub>5</sub>	$r^2 = 0.02, p = 0.56$	$r^2 = 0.46, p < 0.05$	$r^2 = 0.11, p = 0.14$	$r^2 < 0.01, p = 0.76$	$r^2 = 0.12, p = 0.13$	$r^2 = 0.13, p = 0.12$

**Table 1:** Regressions of known quantities of oxides and elements via WD-XRF versus corrected  $\mu$ XRF data with methods ranked first in order of coefficient of determination then by number of p values  $< 0.05$  (in bold).  $n = 20$  for all  $r^2$  values. Titanium, silicon and zircon normalisation had  $r^2 < 0.5, p > 0.05$  in all cases and are not shown. cts/s:  $\mu$ XRF counts per second.

To identify the main directions of variation in the Fern Gully inorganic data, a principal component analysis (PCA) was performed using the vegan package (Oksanen et al., 2018) in RStudio (Team-RStudio, 2015; Ihaka and Gentleman, 2016). A subset of seven normalised elements comprising those with the highest counts per second (silicon, iron, calcium, bromine, zircon, potassium and titanium), along with LOI estimated organic content were used. A broken stick model was used to estimate the number of significant components in the  $\mu$ XRF record (Fig. S2) (Baczkowski, 2000). The PCA vectors were scaled by the species scores before being divided by the standard deviation of each element and multiplied by an equalising constant. In this way, element vectors were centred and standardised so that the relative variance of each element could be compared.

To characterise possible local sediment end members, samples were taken from the following locations:

- The surface of modern dunes ~30 m from the edge of Fern Gully Lagoon and ~30 m from the edge of nearby Welsby Lagoon.
- Sand three meters below the surface of dunes surrounding Fern Gully Lagoon.
- The surface of outflow one at Fern Gully Lagoon (Fig. 1c).
- Local rock outcrops (Point Lookout rhyolite and Dunwich sandstone).
- An indurated layer representing the B horizon of material below each of the two lagoons.

These endmember samples were scanned using Itrax  $\mu$ XRF and placed on the PCA using the vegan predict model (Oksanen et al., 2018).

### 3.4 Dating

A preliminary age obtained from Fern Gully Lagoon exceeded the radiocarbon dating limit of ~50 ka (Tibby et al., 2017). As such, we employed two dating methods to examine different depths of the core in this study:  $^{14}\text{C}$  dating for sediments to a depth of 288 cm, and single-grain OSL dating from 171 cm to the base of the core. Four paired OSL and  $^{14}\text{C}$  samples were collected between 171 and 288 cm, to assess age agreement.

$^{14}\text{C}$  dating was performed on 18 macrofossil samples, including seeds, leaf material, and bark and charcoal > 3 mm diameter. Six paired  $^{14}\text{C}$  samples were collected from different materials to identify any offset due to material properties, including absorption of humic acids and alteration by ground water residence time (Hofmann et al., 2019). Sample preparation was undertaken at the Australian Nuclear Science and Technology Organisation, where each of the samples was dissected under a stereoscope. Any identified root fragments or other foreign objects were removed. Each sample then underwent an Acid-Base-Acid (ABA) pre-treatment to remove humic acids, following Brock et al. (2010) and were freeze-dried before graphitisation and AMS measurement. After correction for isotopic fractionation using measured  $\delta^{13}\text{C}$  values, the conventional  $^{14}\text{C}$  ages were calibrated using the Southern Hemisphere Calibration Curve (SHCal13; Hogg et al. 2013).

Single-grain OSL dating was performed on 19 quartz samples collected from core sections with the highest inorganic content. The sediment samples were extracted under filtered and subdued red LED lighting, where ~12 g of bulk sediment (dry weight) was retained from the exposed core face and margins for beta and gamma dose rate determination and beta dose rate water correction (after oven drying at 100°C). Additional bulk sediment was collected from the overlying and underlying 10 cm depth of each OSL sample position for gamma dose rate determination and gamma dose rate water content correction. Single-grain equivalent dose ( $D_e$ ) measurements and environmental dose rate assessments were made using the experimental procedures described by

Demuro et al. (2013; 2015). Further details of the OSL methodologies employed in this study, including SAR suitability assessments (dose recoveries) and quality assurance criteria, are included in the supplementary materials.

The age-depth model for Fern Gully Lagoon was constructed from the  $^{14}\text{C}$  and OSL likelihoods using a Bayesian Poisson process depositional model in OxCal v4.2.4 (P\_Sequence model: Bronk-Ramsey, (2009); Bronk-Ramsey and Lee, (2013)), which allows for randomly variable deposition rates through the age-depth profile. The P\_Sequence  $k_0$  base rigidity parameter, which controls the ability of the model to respond to variations in the prior and likelihood data, was set to a single event per 1 cm of sedimentation but was allowed to vary between 0.01 to 100 events per centimetre to accommodate any major fluctuations in deposition rate. This additional flexibility is at the expense of precision in the final age model and results in a liberal estimate of uncertainties inherent in the data.

As part of the assessment of modelling priors, we used a common method for identifying change in linear records: pruned exact linear time (PELT) multi-changepoint analysis (Killick and Eckley, 2014). PELT was performed on the sediment inorganic content record and the  $\mu\text{XRF}$  Si, Ti, K and Zr data to identify any statistically significant changes in deposition mode, including potential sedimentation hiatuses (see supplementary material for further details and results). These independently assigned changepoint locations were used to identify separate depositional units in the OxCal modelling framework (Fig. 3, S3), each of which was represented by a separate P\_Sequence with delineating start and end boundaries, nested within a master Sequence according to stratigraphic priors. Posterior dated events were automatically calculated at 1 cm intervals throughout the sequence. Further details of the Bayesian age-depth modelling method are included in the supplementary materials.

## 4. Results

### 4.1 Core correlation

Sequence slotting revealed that the top of the two cores were vertically offset by ~97 cm, rather than the 50 cm planned (Fig. 2). The unplanned offset meant that a total of 15 cm of sediment located at the end of several core drives was not recovered, with the largest contiguous gap being 4 cm. These lost sections did not coincide with the boundaries defined using change-point analysis.

### 4.2 $\mu$ XRF normalisation and calibration

Eight of the twelve elements from the  $\mu$ XRF Fern Gully Lagoon sequence had significant correlations (at  $p < 0.05$ ) with the WD-XRF samples when normalised by total counts per second, with the four best correlated elements returning a coefficient of determination of  $r^2 > 0.8$ ,  $p < 0.05$  (Table 1, Fig. S1). Normalisation via titanium, silicon or zircon was largely unsuccessful ( $r^2 < 0.5$ ). Of the remaining 21 recorded elements not included in WD-XRF regressions, 14 could not be considered representative of elemental concentration either due to low mean counts per second (Striberger et al., 2010; van der Bilt et al., 2015) or having >5% of data with zero values (Sáez et al., 2009).

A lack of correlation between the incoherent/coherent scattering ratio and measured water content ( $r^2 = 0.05$ ,  $p < 0.05$ ,  $n = 804$ ) indicated that it was not possible to correct the  $\mu$ XRF record for water content (see Boyle et al., 2015). However, calibration of the  $\mu$ XRF record by conventional XRF accounts for any offset due to water content. Inorganic content estimated by the incoherent/coherent scattering ratio, as used in many recent studies (e.g. Guyard et al., 2007; Jouve et al., 2013; Burrows et al., 2016; Mackenzie et al., 2017), had a very weak relationship ( $r^2 = 0.09$ ,  $p < 0.05$ ) to inorganic content estimated by LOI, possibly due to the very high organic content of the core sequence.

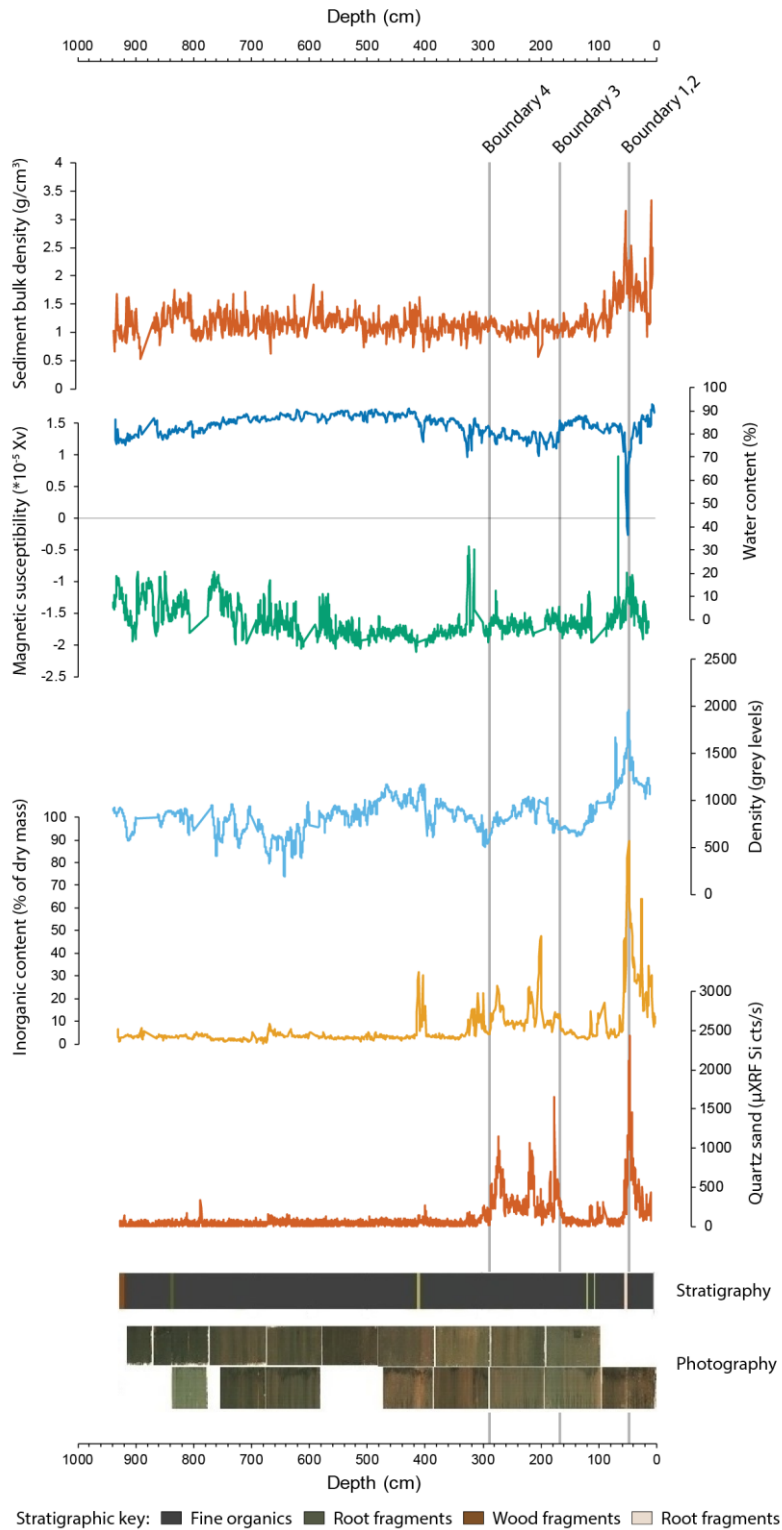


**Figure 3:** Fern Gully Lagoon sediment stratigraphy, visible wavelength photography (brightened to show colour variation), sediment bulk density, water content, magnetic susceptibility, X-radiograph derived relative density, inorganic content and  $\mu$ XRF derived  $\text{SiO}_2$  content. The four depositional boundaries used in the age model were derived from silicon  $\mu$ XRF counts per second (cts/s, section 2.4 and supplementary material)

### 4.3 Fern Gully Lagoon sediment composition

Fern Gully Lagoon sediments are black, finely grained and highly organic, with some macrofossils, such as roots and wood fragments. They have an average of only ~8% inorganic material by dry mass (Fig. 3). Water content is also high, at 36–93% of wet sample weight. Sediment density and water content remained relatively constant down core, with no overall monotonic trend (Fig. 3), demonstrating that there is little compaction of the sediments with increasing overburden pressure.

Both inorganic content and  $\mu$ XRF-derived silicon content exhibit several peaks and a plateau of ~10% inorganic content from ~170–270 cm (Fig. 2). Lower zircon levels in this part of the record likely indicate smaller average grain size (Cuven et al. 2010). There was a strong correlation ( $r^2 = 0.70$ ,  $p < 0.05$ ) between the LOI inorganic content and  $\mu$ XRF-derived silicon, indicating quartz sand is the major inorganic component of the sediment. While the magnetic susceptibility and X-radiograph records indicate variability in the lower part of the record, aligning with photographed banding (Fig. 3), the inorganic content and the  $\mu$ XRF silicon records indicate very little change, with largely consistent low quantities of inorganic material present.

### 4.4 $^{14}\text{C}$ dating

The AMS  $^{14}\text{C}$  ages have a large amount of scatter (Table 2, Fig. 4). In general, the  $^{14}\text{C}$  ages obtained from identifiable terrestrial macrofossils (gum nuts, seeds, leaves and bark fragments) are stratigraphically consistent over the uppermost 2 m of the core ( $n = 7$ ) (Table 2). Three samples collected from below one metre yield very young outliers: sample RC-3 from 115 cm has a modern  $^{14}\text{C}$  age, and samples RC-7 and RC-14 from 159 cm and 215 cm, respectively, produced ages of  $<2$  cal. ka. These three samples were originally identified as reed stalk segments but were subsequently inferred to be root fragments. This re-interpretation was based on roots being identified during further sampling in the same core sections. Additional evidence for localised root penetration is

apparent from some of the single-grain OSL  $D_e$  distributions (section 4.5). Encouragingly, there is a broad agreement between the paired radiocarbon ages obtained at the same depths using terrestrial seeds and terrestrial leaf fragments (Table 2). However, there is an age offset of ~6 kyr for the replicate bark and reed stalk samples collected from a depth of 79 cm. This offset could again be attributed to misidentification of root material at this depth.

Sample ID	Lab ID (ANSTO)	Sample Type	Depth (cm)	$\delta^{13}\text{C}$ (‰)	pMC (%)	Conventional $^{14}\text{C}$ Age ( $^{14}\text{C}$ yr BP)	Calibrated $^{14}\text{C}$ 95.4% probability range (cal. yr BP)
<i>Fern Gully Core 1 (FG15-1)</i>							
FG15 RC-1	OZU189	Terrestrial gum nut	34.5–35.5	-26.0 ± 0.2	87.83 ± 0.31	1,040 ± 30	803–960
FG15 RC-2	OZU190	Terrestrial leaf fragment	34.5–35.5	-26.2 ± 0.1	90.62 ± 0.28	790 ± 30	655–730
FG15 RC-11	OZU792	Terrestrial bark fragment	78.5–79.5	-24.6 ± 0.1	24.52 ± 0.13	11,290 ± 40	13036–13211
FG15 RC-12*	OZU793	Reed stalk segment	78.5–79.5	-24.9 <sup>a</sup>	46.07 ± 0.18	6,225 ± 35	6952–7238
FG15 RC-3*	OZU191	Reed stalk segment	114.5–115.5	-25.7 ± 0.1	128.18 ± 0.61	Modern	Modern
FG15 RC-4	OZU192	Terrestrial seed	134.5–135.5	-24.1 ± 0.1	15.46 ± 0.11	15,000 ± 60	17966–18366
FG15 RC-5	OZU193	Terrestrial leaf fragment	134.5–135.5	-22.6 ± 0.1	16.49 ± 0.11	14,480 ± 60	17392–17849
FG15 RC-13	OZU794	Terrestrial bark fragment	158.5–159.5	-25.0 ± 0.2	13.16 ± 0.10	16,290 ± 60	19422–19870
FG15 RC-14*	OZU795	Reed stalk segment	158.5–159.5	-25.0 <sup>b</sup>	78.69 ± 0.27	1,925 ± 30	1736–1896
FG15 RC-6*	OZU194	Charcoal	174.5–175.5	-28.5 ± 0.1	2.94 ± 0.04	28,330 ± 120	31637–32682
FG15 RC-7*	OZU195	Reed stalk segment	214.5–215.5	-22.1 ± 0.3	97.97 ± 0.55	165 ± 50	Modern–281
FG15 RC-8*	OZU196	Charcoal	224.5–225.5	-26.7 ± 0.1	0.70 ± 0.03	39,880 ± 330	42916–44192
FG15 RC-15**	OZU796	Terrestrial bark fragment	227.5–228.5	-24.6 ± 0.1	0.71 ± 0.07	39,730 ± 810	42343–44960
FG15 RC-16*	OZU797	Charcoal	227.5–228.5	-26.5 ± 0.3	0.35 ± 0.06	45,400 ± 1,500	46377– <sup>c</sup>
FG15 RC-9*	OZU197	Charcoal	234.5–235.5	-27.2 ± 0.1	0.25 ± 0.02	48,200 ± 750	46815–49875
FG15 RC-10*	OZU198	Reed stalk segment	274.5–275.5	-23.4 <sup>a</sup>	2.27 ± 0.07	30,420 ± 240	33945–34803
FG15 RC-17*	OZU798	Charcoal	287.5–288.5	-26.4 ± 0.1	0.41 ± 0.04	44,110 ± 850	45785–49430
FG15 RC-18*	OZU799	Reed stalk segment	287.5–288.5	-26.3 <sup>a</sup>	0.96 ± 0.04	37,300 ± 360	41178–42297

**Table 2:** AMS Radiocarbon ages. \* denotes an age excluded from the age-depth model due to material type, while \*\* denotes an age eliminated from the final Bayesian model as it was identified as a major statistical outlier during initial modelling and prevented successful convergence. <sup>a</sup>  $\delta^{13}\text{C}$  values without associated uncertainty due to a limited number of determinations. <sup>b</sup>  $\delta^{13}\text{C}$  is assumed - measured value was not available. <sup>c</sup> Maximum value beyond calibration range.  $^{14}\text{C}$  ages have been calibrated using the SHCal13 curve (Hogg et al. 2013) in OxCal v4.2.4. The calibrated age range shown is the 95.4% probability range (combining two or more potential calibration ranges, where they exist). All  $\delta^{13}\text{C}$  values relate solely to the graphite derived from the fraction that was used for the radiocarbon measurement and have been derived using EA-IRMS. Uncalibrated  $^{14}\text{C}$  ages have been corrected for isotopic fractionation using their measured  $\delta^{13}\text{C}$  values and are quoted with their 1 $\sigma$  errors.

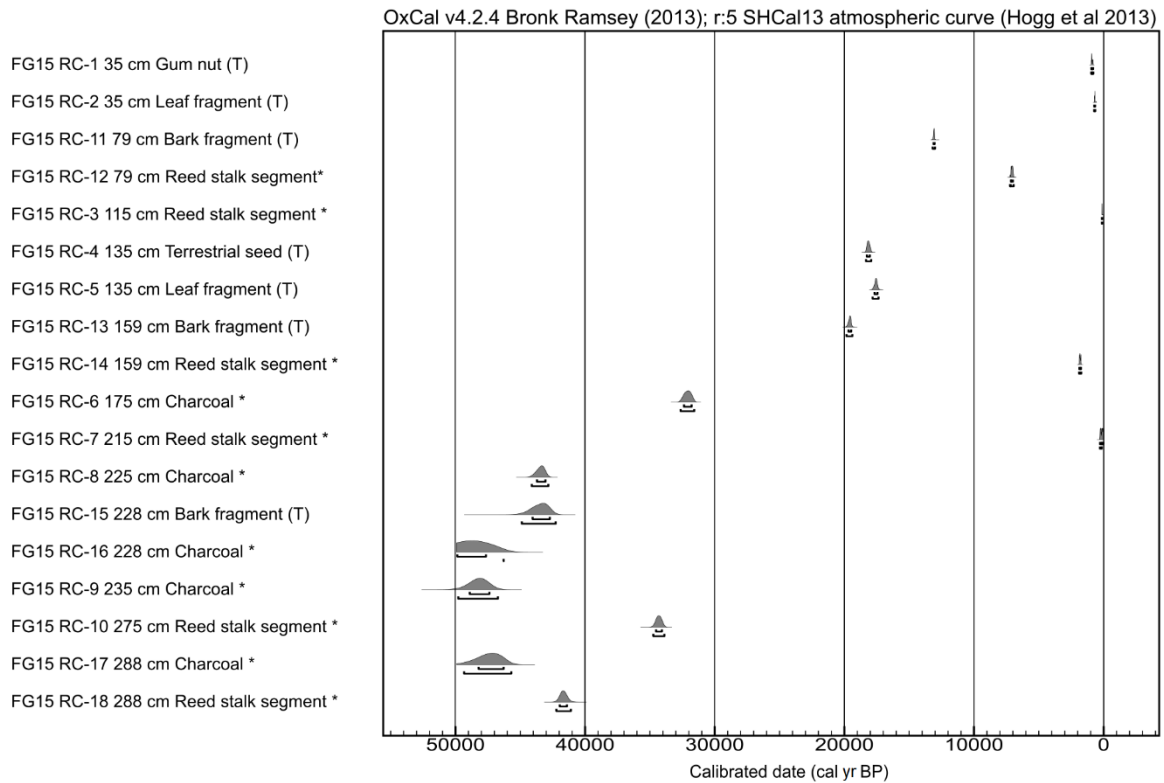


**Figure 4:** Calibrated radiocarbon age probability distributions with calibrated 68.2% and 95.4% age ranges. \* denotes an age excluded from the age-depth model due to material type. (T): a terrestrial source.

Five <sup>14</sup>C samples were single >3 mm charcoal fragments. <sup>14</sup>C dating of charcoal can underestimate sample age in organic-rich wetlands unless prepared using a specific method to remove humic acid contamination (Nilsson et al., 2001; Turetsky et al., 2004; Brock et al., 2011). Contamination is particularly an issue for old samples where small concentrations of humic acid can produce large underestimations (e.g. 1% modern carbon contamination can cause a 15 kyr underestimation in a 50 ka sample) (Brock et al., 2011). As the charcoal samples from Fern Gully Lagoon were prepared using ABA, the resultant ages may have been inadvertently affected by humic acid contamination (Brock et al., 2010). Indeed, there is some evidence to suggest this might be the case for the three charcoal samples collected from depths of 228, 235 and 288 cm, which have statistically indistinguishable 2σ calibrated age ranges (Fig. 4, Table 2).

#### 4.5 OSL dating

The single-grain OSL dating results are summarised in Table 3, with representative single-grain  $D_e$  distributions shown as radial plots in Figure 5. The OSL samples from Fern Gully Lagoon exhibit a broad range of  $D_e$  distribution characteristics, indicative of spatially and temporally variable bleaching and mixing conditions at the site (e.g., Arnold and Roberts, 2009; Arnold et al., 2007, 2008, 2012). Full discussions of the single-grain  $D_e$  distributions and statistical age models used to derive representative burial dose estimates for each sample are provided in the supplementary materials.

The final OSL ages exhibit good stratigraphic consistency for thirteen of the nineteen samples (Table 3). The remaining six samples (FG15 OSL-1, -8, -8-2, -9, -10 and -16) yield very young, outlying and inverted ages of between  $6.69 \pm 2.0$  ka to  $21.2 \pm 2.6$  ka for the lowermost 7 m of the core sequence. These outlying ages in the lowermost 7 m of the core are in keeping with the complex  $D_e$  distribution characteristics observed for the six samples, which are characterised by very high overdispersion values (53–119%) and multiple discrete dose components (Fig. S7). These multimodal  $D_e$  datasets are interpreted as reflecting the presence of locally intruded young grain populations. These populations could potentially be the result of sporadic lake desiccation and the formation of deep surface cracks (a process that is visible today in analogous peat-rich wetlands on NSI) and, or, downward grain transportation via root penetration into older sediments, as has been found previously (e.g. Bateman et al., 2007; Brill et al., 2012). These interpretations are consistent with the presence of modern or near-modern organic remains at depths >1 m in the  $^{14}\text{C}$  study (section 4.4).

Assuming that the multiple discrete dose components of FG15 OSL-1, -8, -8 2, -9, -10 and -16 can be explained by localised post-depositional mixing, it follows that the bulk (sample-average) dose rate of these six samples may not be entirely representative of that experienced by either dose component during burial. Owing to the impracticalities of retrospectively deriving a component-

specific dose rate for the multiple identified components, these samples are not considered suitable for dating. The ages shown for these samples in Table 3 are included for indicative purposes only and have not been included as likelihood estimates in the Bayesian age model.

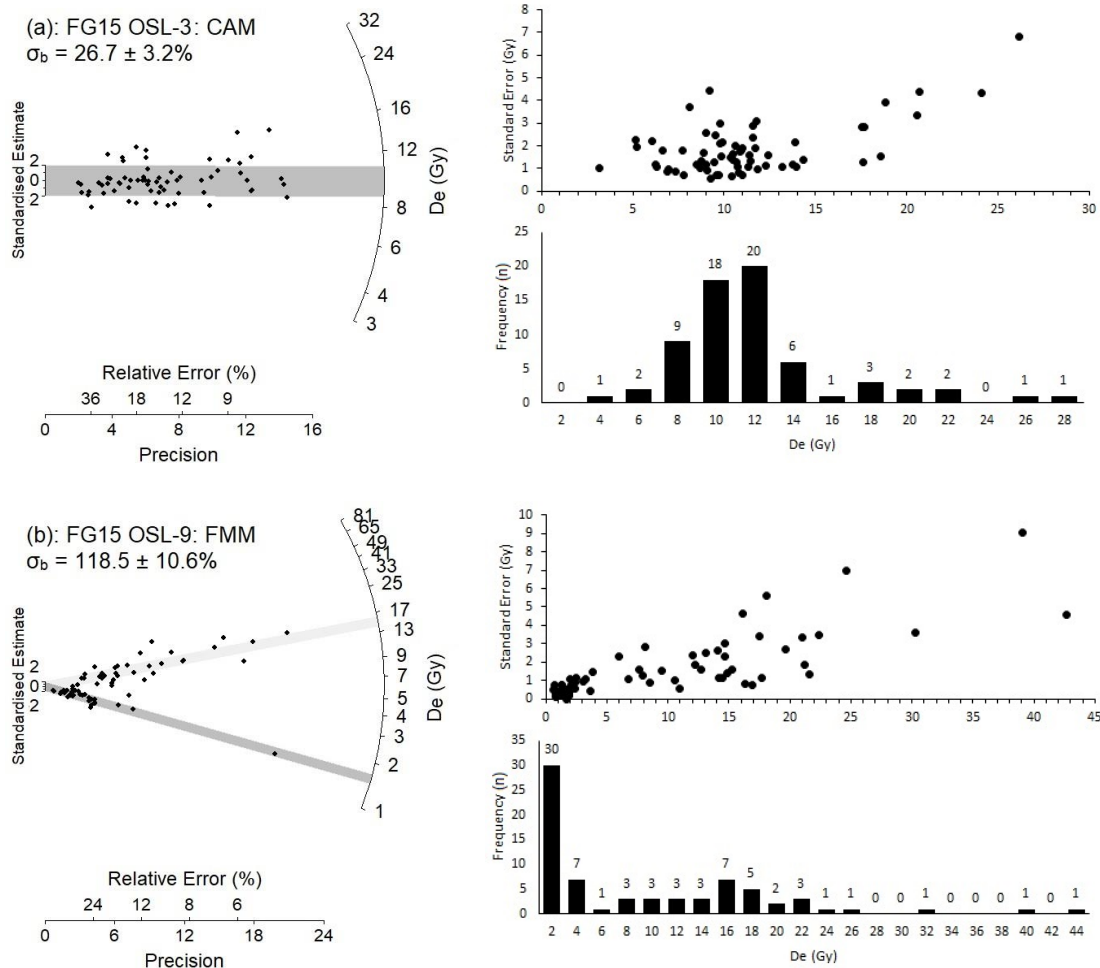


**Figure 5:** Example single-grain  $D_e$  distributions shown as radial plots and frequency histograms with ranked plots of  $D_e$  versus standard error. (a) Samples FG15 OSL-3 (813–832 cm depth), which was considered suitable for dating using the central age model (CAM). The grey bar on the radial plot is centred on the CAM  $D_e$  value used to derive the final burial dose of this sample; (b) Sample FG15 OSL-9 (326–335 cm depth), which was not considered suitable for dating because it contains multiple discrete dose populations, as identified by the finite mixture model (FMM). The two dose components identified by the FMM are shown by the light and dark grey bands in the radial plot. Individual  $D_e$  estimates are presented with their  $1\sigma$  error ranges, which are derived from a random uncertainty term arising from photon counting statistics for each OSL measurement, an empirically determined instrument reproducibility uncertainty of 2.5% (following the approach outlined in Jacobs et al. (2006)) and a dose-response curve fitting uncertainty determined using 1000 iterations of the Monte Carlo method implemented in Analyst (Duller, 2015).

Sample (core)	Depth (cm)	Water Content (% dry weight) <sup>a</sup>	Environmental dose rate (Gy/kyr) <sup>b,c,d,e,f</sup>					Equivalent dose (D <sub>e</sub> ) data			D <sub>e</sub> (Gy) <sup>f</sup>	Final age (ka) <sup>f,j</sup>
			Beta dose rate	Gamma dose rate	Internal dose rate	Cosmic dose rate	Total dose rate	No. of grains <sup>h</sup>	Overdispersion (σ <sub>s</sub> ) (%) <sup>i</sup>	Age Model <sup>g</sup>		
FG15 OSL-18 (1)	171–180	320/404/507	0.03±0.005	0.03±0.0007	0.02±0.007	0.03±0.003	0.11±0.01	102	50.3±4.2	MAM-3	3.60±0.8	33.2±8.0
FG15 OSL-17 (1)	181–190	342/361/497	0.03±0.005	0.03±0.0009	0.02±0.007	0.03±0.003	0.12±0.01	52	50.9±5.8	CAM	9.08±0.7	77.7±9.2
FG15 OSL-16 2 (2)	204–213	386/344/484	0.01±0.003	0.02±0.0006	0.02±0.007	0.03±0.003	0.09±0.01	117	39.5±2.9	MAM-3	14.3±0.6	128±15.3
FG15 OSL-16 (1) <sup>k</sup>	204–213	386/344/484	0.03±0.006	0.027±0.001	0.02±0.007	0.03±0.003	0.11±0.01	50	92.2±10.7	MAM-3	1.48±0.1	13.3±2.0
FG15 OSL-15 (1)	214–223	336/363/477	0.03±0.005	0.03±0.0009	0.02±0.007	0.03±0.003	0.12±0.01	96	41.3±3.6	CAM	11.4±0.5	95.5±9.73
FG15 OSL-14 (1)	235–244	408/378/468	0.02±0.003	0.03±0.0007	0.02±0.007	0.03±0.003	0.09±0.009	33	34.5±5.4	CAM	12.7±0.9	135±16.3
FG15 OSL-13 (1)	263–272	406/399/460	0.02±0.004	0.04±0.008	0.02±0.007	0.03±0.003	0.1±0.01	37	34.0±5.0	CAM	14.7±0.9	132±20.3
FG15 OSL-12 (1)	273–282	362/402/456	0.04±0.007	0.03±0.003	0.02±0.007	0.03±0.003	0.1±0.01	131	34.4±2.5	CAM	16.4±0.5	137±15.4
FG15 OSL-11 (1)	283–292	446/426/456	0.02±0.003	0.02±0.01	0.02±0.007	0.03±0.003	0.09±0.02	82	28.9±2.8	CAM	14.8±0.5	171±33.4
FG15 OSL-10 2 (2)	306–315	545/433/457	0.004±0.001	0.007±0.0003	0.02±0.007	0.03±0.003	0.06±0.008	63	33.2±3.7	CAM	13.8±0.6	179±22.4
FG15 OSL-10 (1) <sup>k</sup>	306–315	545/433/457	0.01±0.003	0.01±0.0005	0.02±0.007	0.03±0.003	0.08±0.009	86	53.3±6.1	MAM-3	1.65±0.1	21.2±2.6
FG15 OSL-9 (1) <sup>k</sup>	326–335	380/450/455	0.01±0.002	0.02±0.003	0.02±0.007	0.03±0.003	0.08±0.009	82	118.5±10.6	MAM-4	1.59±0.1	20.0±2.8
FG15 OSL-8 (1) <sup>k</sup>	405–414	572/673/477	0.009±0.002	0.02±0.0005	0.02±0.007	0.03±0.003	0.08±0.008	80	76.9±8.4	MAM-4	1.40±0.1	19.9±2.7
FG15 OSL-8 2 (2) <sup>k</sup>	405–414	572/673/477	0.02±0.004	0.02±0.0005	0.02±0.007	0.03±0.003	0.08±0.009	51	94.8±10.5	MAM-4	1.48±0.1	17.5±2.3
FG15 OSL-5 (1)	655–674	629/666/578	0.005±0.001	0.003±0.0002	0.02±0.007	0.02±0.002	0.05±0.008	37	39.2±5.7	CAM	12.6±0.7	248±40.6

**Table 3:** Dose rate data, equivalent doses (D<sub>e</sub>), overdispersion values, and OSL ages for lacustrine samples from Fern Gully Lagoon, NSI. The final OSL age of each sample has been calculated by dividing the D<sub>e</sub> value by the total dose rate.

<sup>a</sup> Long-term water contents used for beta / gamma / cosmic-ray dose rate attenuation, expressed as % of dry mass of mineral fraction, with an assigned relative uncertainty of ±10%. The final beta dose rates have been adjusted for moisture attenuation using the average water content from the midpoint of each OSL sample depth. The final gamma dose rates have been adjusted using the water content determined separately for the gamma dose rate bulk sediment samples, which were collected for each OSL sample depth, as well as for the overlying and underlying 10 cm depth. The final cosmic-ray dose rates have been adjusted using the average water content measured from the contiguous 1 cm<sup>3</sup> bulk sediment samples collected throughout the overlying core sequence.

<sup>b</sup> Beta, gamma and internal dose rates have been calculated on dried and powdered sediment samples using ICP-MS and ICP-OES. The beta dose rates have been calculated on bulk sediment samples collected from each OSL sample depth. The gamma dose rates have been determined separately on bulk sediment samples collected for each OSL sample depth, as well as for the overlying and underlying 10 cm depth of each OSL sample position, following De Deckker et al. (2019).

<sup>c</sup> Radionuclide concentrations have been converted to alpha, beta and gamma dose rates using the published conversion factors of Guérin et al. (2011), and allowing for beta-dose attenuation (Mejdahl, 1979; Brennan, 2003) and long-term water content correction (Aitken, 1985).

<sup>d</sup> An internal dose rate of  $0.02 \pm 0.007$  Gy/kyr has been included in the final dose rate calculations of all samples, based on ICP-MS U and Th measurements made on etched quartz grains from associated aeolian deposits at Welsby Lagoon (Lewis et al., in prep) and an alpha efficiency factor ( $a$  value) of  $0.04 \pm 0.01$  (Rees-Jones, 1995; Rees-Jones and Tite, 1997).

<sup>e</sup> Cosmic-ray dose rates were calculated after Prescott and Hutton (1994), and assigned a relative uncertainty of  $\pm 10\%$ .

<sup>f</sup> Mean  $\pm$  total uncertainty (68% confidence interval), calculated as the quadratic sum of the random and systematic uncertainties.

<sup>g</sup> SG OSL = single-grain optically stimulated luminescence; MAM-3 = three-parameter minimum age model (Arnold et al., 2009), MAM-4 = four-parameter minimum age model (Arnold et al., 2009); CAM = Central age model (Galbraith et al., 1999). MAM-3 and MAM-4  $D_e$  estimates were calculated after adding, in quadrature, a relative error of 25% to each individual  $D_e$  measurement error to approximate the underlying dose overdispersion observed in an 'ideal' (well-bleached and unmixed) sedimentary sample from this core (FG15 OSL-3), which is consistent with global overdispersion datasets (Arnold and Roberts, 2009).

<sup>h</sup> Number of  $D_e$  measurements that passed the SAR quality assurance criteria and were used for  $D_e$  determination.

<sup>i</sup> The relative spread in the  $D_e$  dataset beyond that associated with the measurement uncertainties for individual  $D_e$  values, calculated using the CAM.

<sup>j</sup> Total uncertainty includes a systematic component of  $\pm 2\%$  associated with laboratory beta-source calibration.

<sup>k</sup> Samples excluded from the Bayesian model as they contain multiple discrete dose populations when fitted with the FMM (see section 3.5 for details).

#### 4.6 Bayesian age-depth model

Thirteen single-grain OSL ages and eighteen  $^{14}\text{C}$  ages were included in the Bayesian age modelling procedure, separated by three depositional boundaries. A preliminary version of the model tested using these 31 likelihood estimates failed to converge owing to the identification of major statistical outliers. We excluded all potentially inaccurate charcoal and misidentified reed stalk ages from the second model (see Table 2). The youngest charcoal  $^{14}\text{C}$  sample (FG15 RC-6) had an age that was consistent with the OSL sample collected at 175 cm depth (FG15 OSL-18) (see Section 4.2), suggesting that it may not be affected by humic acid contamination. However, for the sake of consistency, it was excluded from further consideration. These quality control measures resulted in only seven of the original eighteen  $^{14}\text{C}$  likelihood estimates being included in the second Bayesian age model. A preliminary version of this model failed to converge owing to the identification of a major statistical outlier (sample FG15 RC-15). It was, therefore, necessary to eliminate this  $^{14}\text{C}$  likelihood estimate in the final Bayesian model.

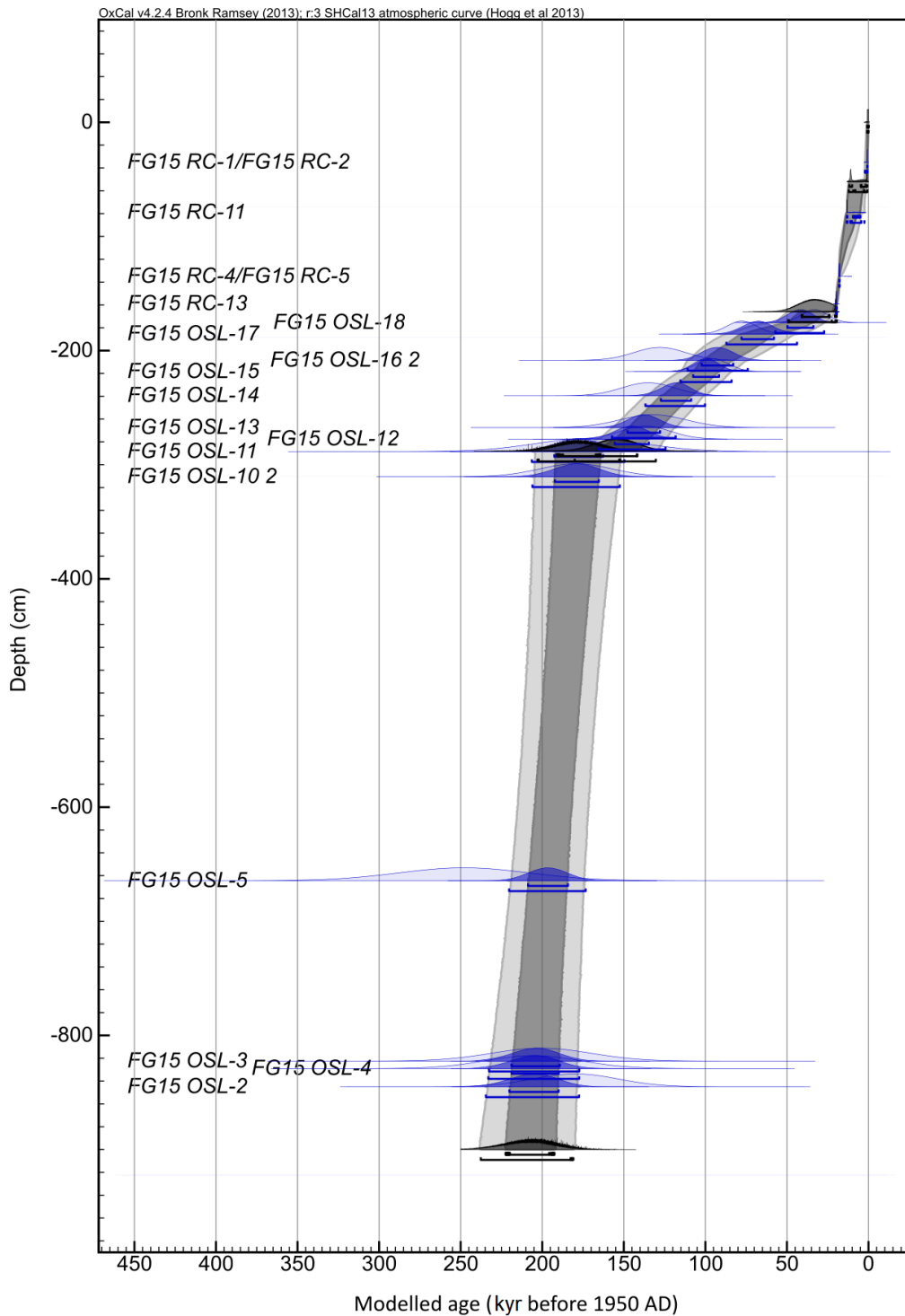


**Figure 6:** Bayesian age/depth model for the Fern Gully Lagoon sequence obtained using a non-continuous deposition scenario. The prior age distributions for the dating samples (likelihoods) are shown in light blue. The modelled posterior distributions for the dating samples and unit boundaries are shown in dark blue and grey, respectively. Likelihood and posterior ages are shown on a calendar year timescale and expressed in years before 1950 AD. The 68.2% and 95.4% ranges of the posterior probabilities are indicated by the light and dark shading.

The Bayesian model for Fern Gully Lagoon has  $A_{\text{model}}$  and  $A_{\text{overall}}$  values of 62.3% and 64.6%, respectively, marginally exceeding the minimum acceptance threshold of 60% and thus indicating a valid model (Bronk Ramsey, 2009). The modelling results are summarised in Table S4 and illustrated in Fig. 6. The final model indicates a basal age of  $209.3 \pm 28.4$  ka ( $\pm 2\sigma$ ) at 900 cm, in agreement with the previously measured basal age of  $208.4 \pm 32.5$  ka on an adjacent preliminary core (Ad13069, Tibby et al. (2017)). The model reveals four distinct sedimentation phases separated by hiatuses: a late MIS 7 to early MIS 6 phase ( $209.3 \pm 28.4$  ka to  $177.5 \pm 25.4$  ka, 930 – 288 cm), a late MIS 6 to late MIS 3 phase ( $155.2 \pm 24.9$  to  $34.7 \pm 14.5$ , 288 – 166 cm), a mid-MIS 2 to mid-Holocene phase ( $20.9 \pm 1.4$  ka to  $6.5 \pm 5.6$  ka, 166 – 52 cm) and a late Holocene phase ( $1.7 \pm 1.0$  ka to  $0.45 \pm 0.4$  ka, 52 – 0 cm) ( $\pm 2\sigma$ , Table S4, Fig. 6). The average sedimentation rates of these four phases are (from bottom to top) 0.20 m/kyr, 0.01 m/kyr, 0.08 m/kyr and 0.31 m/kyr.

#### **4.7 Identifying aeolian and autochthonous wetland sediment**

Broken stick analysis revealed two significant principal components in the  $\mu$ XRF data (Fig. S2), which combined reflect greater than 97% of the variance in the data. Co-varying silicon, titanium, potassium and zircon defined much of PC1. PC1 is very similar to the local aeolian signature identified by McGowan et al. (2008), and we, therefore, associate PC1 with local aeolian input. PC2 was defined by iron and calcium and is likely associated with a secondary aeolian source or internal wetland processes (Fig. 7). Unfortunately, the position of iron and calcium compounds within the sediment may have been altered post-sedimentation, such as by changing redox, rendering the identification of a source material difficult. Inorganic MIS 5 and Holocene sediments from Fern Gully Lagoon are most similar to contemporary local dune surface and subsurface samples, while the closest source material to MIS 7 inorganics is Dunwich sandstone, which contains notable quantities of iron and calcium.

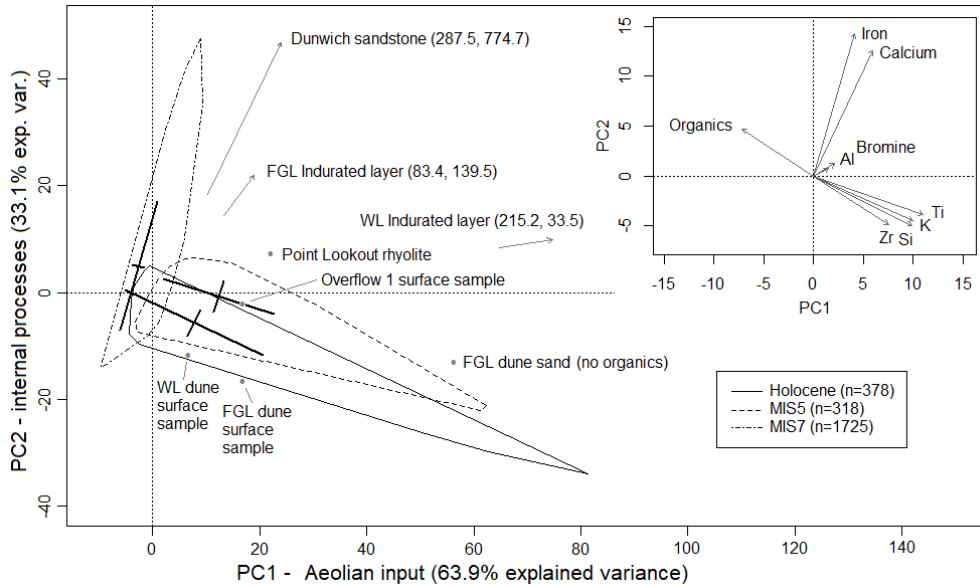


**Figure 7:** PCA biplot of  $\mu$ XRF elements and organic content from Fern Gully Lagoon. Crosses indicate the distribution mean and one standard deviation of the two principal axes of each distribution, while the outer polygon indicates the extent of the samples. Local inorganic source materials are indicated by grey points and grey arrows where these points lie outside the plot. Al.: aluminium; Ti.: titanium; K.: potassium; Si.: silicon; Zr.: zirconium.

#### 4.8 Inorganic sedimentation at Fern Gully Lagoon

The influx of aeolian inorganics was highly variable over the past 209 ka (Fig. 8). Aeolian inorganic input during MIS 7a–c and early MIS 6 ( $209.3 \pm 28.4$  ka to  $177.5 \pm 25.4$  ka) was low while other inorganic sedimentation (represented by calcium and iron dominated inputs) gradually declined. The earliest phase had a high rate of total sedimentation, but no notable inorganic peaks. During the late MIS 6 to late MIS 3 phase ( $155.2 \pm 24.9$  to  $34.7 \pm 14.5$  ka), there were aeolian inorganic peaks at  $\sim 144 \pm 10$  ka (LOI, magnetic susceptibility, PC1),  $\sim 100 \pm 8$  ka (LOI, PC1) and  $\sim 52 \pm 11$  ka (PC1). During the mid-MIS 2 to mid-Holocene phase ( $20.9 \pm 0.8$  to  $6.5 \pm 2.8$  ka), there were some small inorganic peaks from  $\sim 14$ – $11$  ka. Aeolian inorganic sedimentation peaks during the late Holocene, with  $\sim 95\%$  inorganic sediments recorded at  $\sim 1.6 \pm 0.5$  ka (magnetic susceptibility, LOI, PC1). While wetland desiccation and cracking during dry periods, indicated by OSL  $D_e$  distributions, may have displaced quartz sand grains from their original position in the sediment, it is unlikely that this had more than a minor influence on the aeolian inorganic record, as most sediment would have remained intact.

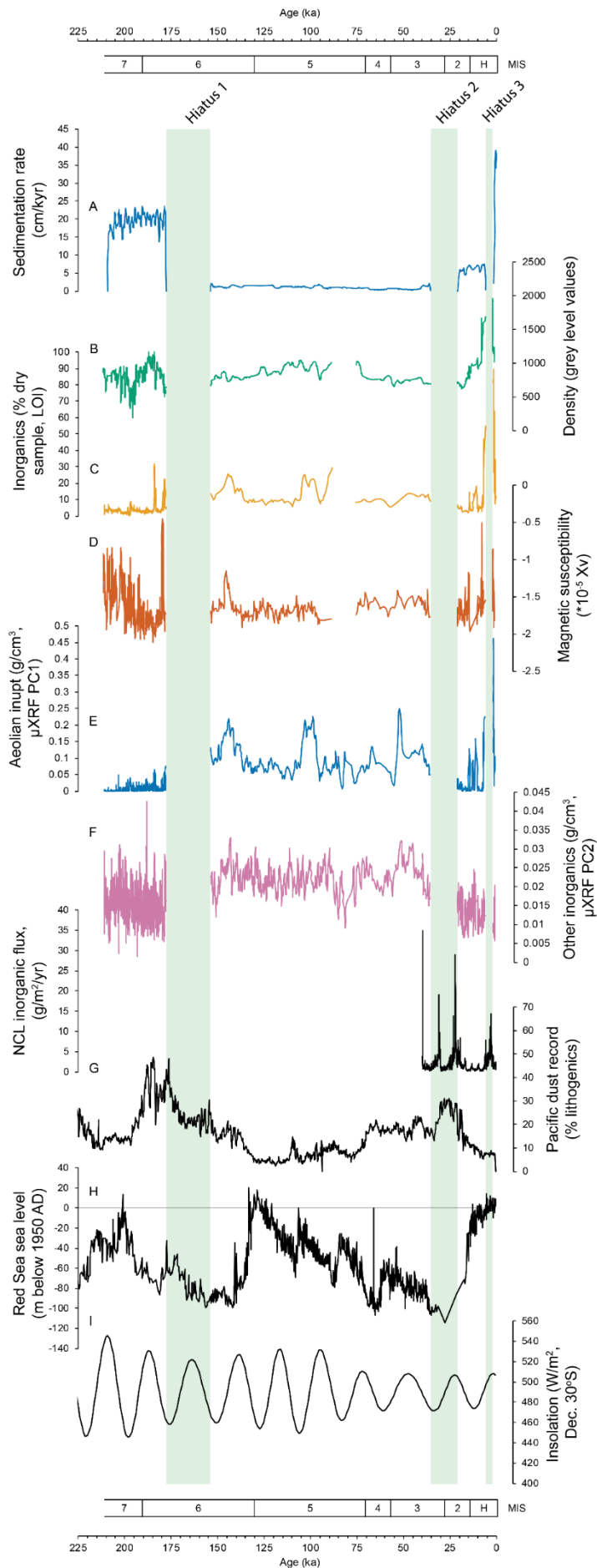


**Figure 8:** Sedimentation rate (3 cm moving average), sediment density (X-radiograph), inorganic content, magnetic susceptibility, calibrated  $\mu\text{XRF}$  aeolian input (silicon, potassium, zircon and titanium, PC1) and other calibrated  $\mu\text{XRF}$  inorganic sedimentation (calcium and iron, PC2). Records for comparison are Native Companion Lagoon (NCL) (Petherick et al., 2008), an Australian dust record from the South Pacific (Lamy et al., 2014), a global sea level record from the Red Sea (Rohling et al., 2009) and December mean insolation for 30 degrees south (Berger and Loutre, 1991)

## 5. Discussion

### 5.1 $\mu$ XRF sediment analysis of highly organic wetlands

The most commonly used  $\mu$ XRF normalisation method (Table S4) – normalisation by total counts per second – was the most suitable for calibrating inorganic elements in the highly organic Fern Gully Lagoon sediments. However, raw counts per second had comparable or better performance than most normalisation methods, indicating that raw data may be used in some circumstances (Table 1). The best performing method for correcting  $\mu$ XRF data appeared to depend on the element(s) under consideration. For example, centred log-ratio correction resulted in the best correlation to WD-XRF particularly for magnesium, bromine and calcium ( $r^2 = 0.85$ ,  $r^2 = 0.84$  and  $r^2 = 0.78$  respectively, where  $p < 0.05$ ,  $n = 20$  for all values), while multiple normalisation methods for aluminium had similarly good  $r^2$  values (0.62 – 0.69, Table 1). For  $\mu$ XRF analysis of highly organic sediments, the optimal method may be to determine the most suitable normalisation method for each element before calibration, rather than using a single normalisation method. If testing of multiple normalisation methods is not possible, centred log-ratio normalisation will produce the best results in the majority of cases, as it has been mathematically proven to counter the closed sum and other distorting effects inherent in  $\mu$ XRF data (Weltje and Tjallingii, 2008; Croudace and Rothwell, 2015).

Several recent palaeoclimate reconstructions from wetland sediments have relied on  $\mu$ XRF derived iron (e.g. Rees et al., 2015; Burrows et al., 2016; Stephens et al., 2018) or magnesium (Foerster et al., 2018) records to infer, for example, waterlogged soils, redox conditions and detrital input. However, our analysis indicates that these elements may not be accurately characterised by  $\mu$ XRF in highly organic sediment. Bromine was used as an indicator of organic content in the Paddy's Lake record (north-western Tasmania), supported by the incoherent to coherent ratio (inc/coh) (Beck et al., 2017). However, while inc/coh and bromine correlate, neither correlated well with organic content in our study ( $r^2 < 0.003$ ,  $p = 0.132$ ,  $n = 804$  and  $r^2 = 0.05$ ,  $p < 0.05$ ,  $n = 804$

respectively). Indeed, the use of inc/coh requires additional stages of calibration to accurately indicate organic content (Woodward and Gadd, 2019). While some recent studies have validated the use of the  $\mu$ XRF inc/coh for estimating organic content (e.g. Field et al., 2018; Woodward et al., 2018), a number have not (e.g. Rees et al., 2015; Turner et al., 2015; Burrows et al., 2016; Pleskot et al., 2018). Standardising normalisation and calibration of  $\mu$ XRF records as a minimum requirement for  $\mu$ XRF derived climate studies would improve record precision and reduce uncertainty in future work.

## **5.2 Dating wetland sediments**

Reliable dating of Australian palaeoclimate sequences that span multiple past interglacial periods has proved difficult, although luminescence dating offers a potentially useful means of filling chronological gaps across a range of palaeoenvironmental contexts (Fu et al., 2017; Roberts et al., 2018; De Deckker et al., 2019). This study highlights the complexities that can be encountered when using single-grain OSL and  $^{14}\text{C}$  dating in organic-rich peaty wetlands. By employing both techniques, it has been possible to better diagnose complications related to material selection (e.g., root fragments and charcoal), post-depositional mixing, and heterogeneous bleaching of sand grains. While a relatively high proportion of the original dating samples were unsuitable for inclusion in the final age model (i.e. 67% of the eighteen  $^{14}\text{C}$  samples and 32% of the nineteen OSL samples), our results highlight the general suitability of  $^{14}\text{C}$  and OSL dating in this depositional context when targeting optimal sampling materials, laboratory protocols and scales of analysis. Careful consideration of dating quality control has proved critical for deriving a meaningful age-depth model at Fern Gully Lagoon. There is good scope for using systematic single-grain OSL dating studies to refine the chronology of other Australian interglacial records.

### 5.3 Fern Gully Lagoon sediment hiatuses

Age-depth modelling indicates that there were three hiatuses in sedimentation at ~177 to 155 ka, ~34.7 to 20.9 ka and 6.5 to 1.7 ka. Palaeoclimate reconstructions from nearby wetland sites on North Stradbroke and Fraser Islands have revealed sedimentary hiatuses during dry periods such as the LGM (Donders et al., 2006; Woltering et al., 2014). Unfortunately, there are no nearby records of sufficient age and resolution to allow comparison of pre-MIS 5 hiatuses at FGL. The timing of two hiatuses in the Fern Gully Lagoon record during mid-MIS 6 and late MIS 3 to mid-MIS 2 are consistent with drier climates observed in a number of Australian records, both in north-east (Kershaw et al., 2007a; Moss and Kershaw, 2007) and central Australia (Fu et al., 2017). The start of the mid-MIS 3 sedimentary hiatus in Fern Gully Lagoon aligns with the commencement of widespread drying of Australia (Kemp et al., 2019), and occurs at the same time as drying in nearby Welsby Lagoon (Cadd et al., 2018). The mid-Holocene hiatus at Fern Gully Lagoon has no equivalent from Welsby Lagoon (Cadd et al., 2018), although Fern Gully Lagoon may be more hydrologically sensitive due to its smaller catchment. Lower rainfall was noted at Swallow Lagoon after ~3 ka (Barr et al., 2019), while mid-Holocene hiatuses or drier phases were recorded at Hidden Lake and Lake Allom on nearby Fraser Island (Longmore, 1997; Donders et al., 2006).

The absence of a hiatus at Welsby Lagoon during the late Holocene after ~3 ka may possibly be due to a fire which burned Fern Gully Lagoon but not Welsby Lagoon. Loss of wetland peat due to fire may exceed 50 cm in a single event (in which a peatland may burn for more than a month) – high peat density and peat moisture content lower than 16% contribute to the loss of greatest material (Ballhorn et al., 2009; Davies et al., 2013; Lukenbach et al., 2015). However, an initial study of sedimentary charcoal did not indicate higher levels during this period (Kemp, unpublished data), and there is no notable change in the calcium record (Fig. 2) which could indicate mineralisation within the sediment as the result of a major peat fire (Smith et al., 2001). Therefore, it is more likely

that Fern Gully Lagoon is more hydrologically sensitive than Welsby Lagoon, and drying led to a late-Holocene hiatus, rather than loss of peat due to a major fire event.

#### **5.4 Palaeoclimate interpretation and comparison with other records**

We interpret increased aeolian inorganic sedimentation in Fern Gully Lagoon as indicative of dry climates, as reduced vegetation cover increases local wind erosion (McGowan et al., 2008).

While changes in wind strength could also be a major source of changing inorganic flux, records of terrestrial dust grain size from the Tasman Sea indicate that regional wind strength was secondary to continental drying in explaining regional aeolian inorganic transport (Hesse and McTainsh, 2003).

Increased biomass burning on NSI is a possible additional driver for increased inorganic sedimentation. However, macrocharcoal and the proportion of sediment inorganic matter are uncorrelated at Fern Gully Lagoon ( $r^2 = 0.04$ ,  $p > 0.05$ ,  $n = 632$  (Kemp, unpublished data)), a situation similar to nearby Welsby Lagoon (Barr et al., 2017). Hence, it appears that increased biomass burning did not play a large role in increasing wind erosion on NSI. Sea-level transgression does not appear to drive inorganic flux to Fern Gully Lagoon as the major marine transgressions during late MIS 6 and after the LGM do not coincide with increased inorganic flux (Fig. 8). However, the lack of inorganic sediment immediately after the LGM may also be due to a change in the dominant regional wind direction which deposited sands offshore as postulated by Walker et al., (2018).

We compared our results to the ~33 kyr inorganic flux record from Native Companion Lagoon (McGowan et al., 2008; Petherick et al., 2008) (Fig. 8) and the ~37 kyr record from Tortoise Lagoon (Petherick et al., 2017). The NCL record indicates that a dry phase occurred during the LGM as well as an increase in inorganic sedimentation at ~3 ka (McGowan et al., 2008). While Tortoise Lagoon records a similar LGM peak, there is no increase late-Holocene inorganic sedimentation (Petherick et al., 2017). The LGM inorganic peak was not recorded at Fern Gully Lagoon due to a hiatus, the LGM hiatus itself indicates that Fern Gully Lagoon was similarly dry.

The Fern Gully Lagoon sequence recorded low aeolian sedimentation with low PC1 scores and the lowest inorganic content ( $\sim 3\%$ ), during MIS 7a–c, indicating that it was likely the wettest interglacial of the past three in subtropical eastern Australia. This finding is similar to the record of moisture availability from central Australia, where recorded lake levels reached their highest for the past  $\sim 250$  ka (Fu et al., 2017); Lynch’s Crater in north-east Australia, where there were wet climates with open water present (Kershaw et al., 2007b), and Naracoorte caves in south-east Australia, where pronounced periods of calcitic growth occurred (Ayliffe et al., 1998). In comparison, there was greater aeolian input during MIS 5, indicating a drier local climate than in MIS 7a–c (Fig. 8; MIS 5 average  $\sim 0.24$  kg/m<sup>2</sup>/kyr vs average  $\sim 0.14$  kg/m<sup>2</sup>/kyr inorganics). The record also contains a notable MIS 5 dry period at  $100 \pm 15.6$  ka. A similar comparatively drier mid-MIS 5b–d from  $\sim 110$ – $90$  ka has been observed in other regions, most notably in tropical north-east Australia (Kershaw et al., 2007a). Conversely, central Australian lakes maintained shallow to deep-water conditions during MIS 5 (Bowler et al., 1998, Fu et al., 2017), while calcite growth occurred after  $\sim 105$  ka (Ayliffe et al., 1998).

During the Holocene, inorganic aeolian deposition at Fern Gully Lagoon averaged  $\sim 0.96$  kg/m<sup>2</sup>/kyr, four times greater than during MIS 5 and almost seven times MIS 7 levels. Greater inorganic flux, in combination with high PC1 scores, suggests the Holocene is the driest interglacial of the last three for subtropical eastern Australia. A drier Holocene relative to MIS 7a–c and MIS 5 is observed in several other Australian records, either via increased dry forest and herbaceous vegetation (Harle et al., 2002; Moss and Kershaw, 2007) or lower flows and lake filling (Maroulis et al., 2007; Nanson et al., 2008; Fu et al., 2017). Holocene drying has been attributed to increasing El Niño frequency compared to past interglacials (Moss and Kershaw, 2007), or to the extended period of high sea levels during the Holocene limiting WPWP influence on monsoonal precipitation and the warm East Australian Current (Nanson et al., 2008). Holocene inorganic sedimentation at Fern Gully Lagoon may also be influenced by human-induced biomass burning. There is a long record of human activity on the island (Neal and Stock, 1986) which may have also contributed to mobilisation of

dune sands. However, the paucity of dated archaeology close to Fern Gully Lagoon currently precludes an assessment of human influence on the Fern Gully record.

The pattern of increasingly dry interglacials observed at Fern Gully Lagoon since MIS 7 is consistent with the few other Australian records covering this period, most notably in central Australia (Bowler et al., 2001; Cohen et al., 2015; Fu et al., 2017), but also in the north (Bowler et al., 1998) and south-east (Edney et al., 1990) of the continent. However, records from eastern Australia – tropical Lynch’s Crater (Kershaw et al., 2007a) and alpine, temperate, Caledonia Fen (Kershaw et al., 2007b) – indicate similar climates during the Holocene and MIS 5. Similar climates between the north-eastern Lynch’s Crater and Fern Gully Lagoon may be explained by the behaviour of the East Australian Current (EAC). SST records from the Tasman Sea, which record the passage of the EAC, indicate similar temperatures for MIS 5e and the Holocene (Kawagata, 2001) as a result of more southerly penetration of the EAC. The more southerly penetration of the EAC may, in turn, may have driven convective rainfall in subtropical and temperate eastern Australia somewhat independent of major continental climate drivers such as ENSO.

## **6. Conclusions**

Analysis of a new discontinuous sedimentary record from Fern Gully Lagoon using  $^{14}\text{C}$  dating, single-grain OSL dating and  $\mu\text{XRF}$  core scanning has enabled the reconstruction of a regional palaeoclimate sequence spanning the last three interglacial complexes. An evaluation of  $\mu\text{XRF}$  normalisation methods indicated that normalisation by total counts per second was the best method for Fern Gully Lagoon sediments.

The elemental signature of increased aeolian input to Fern Gully Lagoon, associated with drier climates, was characterised by PCA. The record indicates a relatively wet MIS 7a–c and early MIS 6 phase, a relatively drier MIS 5 interglacial complex, MIS 4 and MIS 3, and a wetter late MIS 2 which transitioned into a drier Holocene. There is general agreement between the Fern Gully Lagoon

record and central Australian lake records fed by the Australasian monsoon and records from the north- and south-east of the continent. Differences between ENSO driven north-eastern Australian records, and Fern Gully Lagoon may be due to the influence of the East Australian Current.

The increasingly dry interglacials observed from Fern Gully Lagoon may be due to more frequent El Niño events. Understanding how ENSO changes during interglacials is important in predicting future water availability due to climate change, as well as ecosystem response to increasing global temperatures. However, due to limited climate records, further study is required. The Fern Gully Lagoon record, which is sensitive to changing ENSO, may assist in answering some of these questions.

It is difficult to isolate a detailed record of hydrological change without considering changing vegetation types and biomass burning records. Ongoing analysis of multiple climate proxies such as pollen, charcoal and stable isotopes from Fern Gully Lagoon will likely result in a greater understanding of past interglacial climates and their drivers.

## **7. Acknowledgements**

We acknowledge Minjerribah (NSI) and the surrounding waters as Quandamooka Country, and we thank the Quandamooka Yoolooburrabee Aboriginal Corporation for their support of this research. This project was supported by the Australian Research Council Discovery Project DP150103875 and Future Fellowship Project FT130100195. Radiocarbon dating and Itrax  $\mu$ XRF scanning were achieved with the support of AINSE grant ALNGRA16003. We would like to thank Cameron Schulz (DES) and Dr Harald Hofmann (UQ) for field assistance, and the Queensland Government for the Fern Gully Lagoon topographic map. We would also like to thank Mark Raven for WD-XRF analysis and Dr Katherine Grant for support running centred log-ratio calibration on Itrax data, as well as Chester Willard for his useful contributions to the discussion.

## 8. References

- Aitken, M.J., 1985. Thermoluminescence dating. Academic press.
- Arnold, L.J., Bailey, R.M., Tucker, G.E., 2007. Statistical treatment of fluvial dose distributions from southern Colorado arroyo deposits. *Quaternary Geochronology* 2, 162-167.
- Arnold, L.J., Demuro, M., Navazo, M., Benito-Calvo, A., Pérez-González, A., 2012. OSL dating of the Middle Palaeolithic Hotel California site, Sierra de Atapuerca, north-central Spain. *Boreas* 42, 285-305.
- Arnold, L.J., Roberts, R.G., 2009. Stochastic modelling of multi-grain equivalent dose ( $D_e$ ) distributions: Implications for OSL dating of sediment mixtures. *Quaternary Geochronology* 4, 204-230.
- Arnold, L.J., Roberts, R.G., Galbraith, R.F., DeLong, S.B., 2009. A revised burial dose estimation procedure for optical dating of young and modern-age sediments. *Quaternary Geochronology* 4, 306-325.
- Arnold, L.J., Roberts, R.G., MacPhee, R.D.E., Willerslev, E., Tikhonov, A.N., Brock, F., 2008. Optical dating of perennially frozen deposits associated with preserved ancient plant and animal DNA in north-central Siberia. *Quaternary Geochronology* 3, 114-136.
- Ayliffe, L.K., Marianelli, P.C., Moriarty, K.C., Wells, R.T., McCulloch, M.T., Mortimer, G.E., Hellstrom, J.C., 1998. 500 ka precipitation record from southeastern Australia: Evidence for interglacial relative aridity. *Geology* 26, 147-150.
- Baczkowski, A.J., 2000. The broken-stick model for species abundances: An initial investigation. Internal Report STAT 00/10, University of Leeds, UK, 2-25.
- Bailey, R.M., Arnold, L.J., 2006. Statistical modelling of single grain quartz  $D_e$  distributions and an assessment of procedures for estimating burial dose. *Quaternary Science Reviews* 25, 2475-2502.
- Ballhorn, U., Siegert, F., Mason, M., Limin, S., 2009. Derivation of burn scar depths and estimation of carbon emissions with LIDAR in Indonesian peatlands. *Proceedings of the National Academy of Sciences* 106, 21213.

Barr, C., Tibby, J., Leng, M.J., Tyler, J.J., Henderson, A.C.G., Overpeck, J.T., Simpson, G.L., Cole, J.E., Phipps, S.J., Marshall, J.C., McGregor, G.B., Hua, Q., McRobie, F.H., 2019. Holocene El Niño–Southern Oscillation variability reflected in subtropical Australian precipitation. *Scientific Reports* 9, 1627.

Barr, C., Tibby, J., Moss, P.T., Halverson, G.P., Marshall, J.C., McGregor, G.B., Stirling, E., 2017. A 25,000-year record of environmental change from Welsby Lagoon, North Stradbroke Island, in the Australian subtropics. *Quaternary International* 449, 106-118.

Bateman, M.D., Boulter, C.H., Carr, A.S., Frederick, C.D., Peter, D., Wilder, M., 2007. Preserving the palaeoenvironmental record in Drylands: Bioturbation and its significance for luminescence-derived chronologies. *Sedimentary Geology* 195, 5-19.

Beck, K.K., Fletcher, M.-S., Gadd, P.S., Heijnis, H., Jacobsen, G.E., 2017. An early onset of ENSO influence in the extra-tropics of the southwest Pacific inferred from a 14,600 year high resolution multi-proxy record from Paddy's Lake, northwest Tasmania. *Quaternary Science Reviews* 157, 164-175.

Berger, A., Crucifix, M., Hodell, D.A., Mangili, C., McManus, J.F., Otto-Bliesner, B., Pol, K., Raynaud, D., Skinner, L.C., Tzedakis, P.C., Wolff, E.W., Yin, Q.Z., Abe-Ouchi, A., Barbante, C., Brovkin, V., Cacho, I., Capron, E., Ferretti, P., Ganopolski, A., Grimalt, J.O., Hönisch, B., Kawamura, K., Landais, A., Margari, V., Martrat, B., Masson-Delmotte, V., Mokeddem, Z., Parrenin, F., Prokopenko, A.A., Rashid, H., Schulz, M., Riveiros, N.V., 2015. Interglacials of the last 800,000 years. *Reviews of Geophysics* 54, 162-219.

Berger, A., Loutre, M.F., 1991. Insolation values for the climate of the last 10 million years. *Quaternary Sciences Reviews* 10, 297-317.

Berntsson, A., Rosqvist, G.C., Velle, G., 2014. Late-Holocene temperature and precipitation changes in Vindelfjällen, mid-western Swedish Lapland, inferred from chironomid and geochemical data. *Holocene* 24, 78-92.

BOM, 2005. Australian Köppen climate classifications based on a standard 30 year climatology (1961-1990). Bureau of Meteorology, Commonwealth of Australia.

Bostock, H.C., Opdyke, B.N., Gagan, M.K., Kiss, A.E., Fifield, L.K., 2006. Glacial/interglacial changes in the East Australian current. *Climate Dynamics* 26, 645-659.

Bouchard, F., Francus, P., Pienitz, R., Laurion, I., 2011. Sedimentology and geochemistry of thermokarst ponds in discontinuous permafrost, subarctic Quebec, Canada. *Journal of Geophysical Research: Biogeosciences* 116.

Bowler, J.M., Duller, G.A.T., Perret, N., Prescott, J.R., Wyrwoll, K.-H., 1998. Hydrologic changes in monsoonal climates of the last glacial cycle: stratigraphy and luminescence dating of Lake Woods, N.T. Australia. *Paleoclimates* 3, 179-207.

Bowler, J.M., Wyrwoll, K.-H., Lu, Y., 2001. Variations of the northwest Australia summer monsoon over the last 300,000 years: The paleohydrological record of the Gregory (Mulan) Lakes system. *Quaternary International* 82-85, 63-80.

Boyle, J.F., Chiverrell, R.C., Schillereff, D., 2015. Approaches to Water Content Correction and Calibration for  $\mu$ XRF Core Scanning: Comparing X-ray Scattering with Simple Regression of Elemental Concentrations, in: Croudace, I.W., Rothwell, R.G. (Eds.), *Micro-XRF Studies of Sediment Cores, Developments in Paleoenvironmental Research*. Springer Science and Business Media, Dordrecht.

Brennan, B.J., 2003. Beta doses to spherical grains. *Radiation Measurements* 37, 299-303.

Brill, D., Klasen, N., Jankaew, K., Brückner, H., Kelletat, D., Scheffers, A., Scheffers, S., 2012. Local inundation distances and regional tsunami recurrence in the Indian Ocean inferred from luminescence dating of sandy deposits in Thailand. *Natural Hazards and Earth System Sciences* 12, 2177-2192.

Brock, F., Higham, T., Ditchfield, P., Ramsey, C.B., 2010. Current Pretreatment Methods for AMS Radiocarbon Dating at the Oxford Radiocarbon Accelerator Unit (ORAU). *Radiocarbon* 52, 103-112.

Brock, F., Lee, S., Housley, R.A., Ramsey, B., 2011. Variation in the radiocarbon age of different fractions of peat: A case study from Ahrenshöft, northern Germany. *Quaternary Geochronology* 6, 550-555.

Bronk Ramsey, C., 2009. Bayesian Analysis of Radiocarbon Dates. *Radiocarbon* 51, 337-360.

Bronk Ramsey, C., Lee, S., 2013. Recent and Planned Developments of the Program OxCal. *Radiocarbon* 55, 720-730.

Brumsack, H.-J., 2006. The trace metal content of recent organic carbon-rich sediments: Implications for Cretaceous black shale formation. *Palaeogeography, Palaeoclimatology, Palaeoecology* 232, 344-361.

Burrows, M.A., Heijnis, H., Gadd, P., Haberle, S.G., 2016. A new late Quaternary palaeohydrological record from the humid tropics of northeastern Australia. *Palaeogeography, Palaeoclimatology, Palaeoecology* 451, 164-182.

Cadd, H., Tibby, J., Barr, C., Tyler, J., Unger, L., Leng, M., Marshall, J., McGregor, G., Lewis, R., Arnold, L., Lewis, T., Baldock, J., 2018. Development of a southern hemisphere subtropical wetland (Welsby Lagoon, south-east Queensland, Australia) through the last glacial cycle. *Quaternary Science Reviews* 202, 53-65.

Clark, M., Hounslow, M., 2009. CPLSlot Version 2.4b, Monash University, Victoria, Australia.

Cohen, T.J., Jansen, J.D., Gliganic, L.A., Larsen, J.R., Nanson, G.C., May, J.-H., Jones, B.G., Price, D.M., 2015. Hydrological transformation coincided with megafaunal extinction in central Australia. *Geology* 43, 195-199.

Colhoun, E.A., Pola, J.S., Barton, C.E., Heijnis, H., 1999. Late Pleistocene vegetation and climate history of Lake Selina, western Tasmania. *Quaternary International* 57–58, 5–23.

Croudace, I.W., Rindby, A., Rothwell, R.G., 2006. ITRAX: description and evaluation of a new multi-function X-ray core scanner. Geological Society, London, Special Publications 267, 51.

Croudace, I.W., Rothwell, R.G., 2015. *Micro-XRF Studies of Sediment Cores: Applications of a non-destructive tool for the environmental sciences*. Springer.

Cuven, S., Francus, P., Lamoureux, S., 2010. Estimation of grain-size variability with micro X-ray fluorescence in laminated lacustrine sediments, cape bounty, Canadian High Arctic. *Journal of Paleolimnology* 44, 803–817.

Davies, G.M., Gray, A., Rein, G., Legg, C.J., 2013. Peat consumption and carbon loss due to smouldering wildfire in a temperate peatland. *Forest Ecology and Management* 308, 169-177.

De Deckker, P., Arnold, L.J., van der Kaars, S., Bayon, G., Stuut, J.-B.W., Perner, K., Lopes dos Santos, R., Uemura, R., Demuro, M., 2019. Marine Isotope Stage 4 in Australasia: A full glacial culminating

65,000 years ago – Global connections and implications for human dispersal. *Quaternary Science Reviews* 204, 187-207.

Demuro, M., Arnold, L.J., Froese, D.G., Roberts, R.G., 2013. OSL dating of loess deposits bracketing Sheep Creek tephra beds, northwest Canada: Dim and problematic single-grain OSL characteristics and their effect on multi-grain age estimates. *Quaternary Geochronology* 15, 67-87.

Demuro, M., Arnold, L.J., Parés, J.M., Sala, R., 2015. Extended-range luminescence chronologies suggest potentially complex bone accumulation histories at the Early-to-Middle Pleistocene palaeontological site of Huéscar-1 (Guadix-Baza basin, Spain). *Quaternary International* 389, 191-212.

Donders, T.H., Wagner, F., Visscher, H., 2006. Late Pleistocene and Holocene subtropical vegetation dynamics recorded in perched lake deposits on Fraser Island, Queensland, Australia. *Palaeogeography, Palaeoclimatology, Palaeoecology* 241, 417-439.

Duller, G., 2015. The Analyst software package for luminescence data: overview and recent improvements. *Ancient TL* 33, 35-42.

Edney, P.A., Kershaw, A.P., Deckker, P.D., 1990. A late Pleistocene and Holocene vegetation and environmental record from Lake Wangoom, Western Plains of Victoria, Australia. *Palaeogeography, Palaeoclimatology, Palaeoecology* 80, 325-343.

Eggenberger, S., Gobet, E., Leeuwen, J., Schwörer, C., Knaap, W., Dobben, H., Vogel, H., Tinner, W., Rambeau, C., 2018. Millennial multi-proxy reconstruction of oasis dynamics in Jordan, by the Dead Sea. *The Journal of Quaternary Plant Ecology, Palaeoclimate and Ancient Agriculture - Official Organ of the International Work Group for Palaeoethnobotany* 27, 649-664.

Elderfield, H., Ferretti, P., Greaves, M., Crowhurst, S., McCave, I.N., Hodell, D., Piotrowski, A.M., 2012. Evolution of Ocean Temperature and Ice Volume Through the Mid-Pleistocene Climate Transition. *Science* 337, 704-709.

Falster, G., Tyler, J., Grant, K., Tibby, J., Turney, C., Löhr, S., Jacobsen, G., Kershaw, A.P., 2018. Millennial-scale variability in south-east Australian hydroclimate between 30,000 and 10,000 years ago. *Quaternary Science Reviews* 192, 106-122.

Field, E., Tyler, J., Gadd, P.S., Moss, P., McGowan, H., Marx, S., 2018. Coherent patterns of environmental change at multiple organic spring sites in northwest Australia: Evidence of

Indonesian-Australian summer monsoon variability over the last 14,500 years. *Quaternary Science Reviews* 196, 193-216.

Foerster, V., Deocampo, D.M., Asrat, A., Gunter, C., Junginger, A., Kramer, K.H., Stroncik, N.A., Trauth, M.H., 2018. Towards an understanding of climate proxy formation in the Chew Bahir basin, southern Ethiopian Rift. *Palaeogeography, Palaeoclimatology, Palaeoecology* 501, 111.

Fu, X., Cohen, T.J., Arnold, L.J., 2017. Extending the record of lacustrine phases beyond the last interglacial for Lake Eyre in central Australia using luminescence dating. *Quaternary Science Reviews* 162, 88-110.

Gagan, M.K., Ayliffe, L.K., Beck, J.W., Cole, J.E., Druffel, E.R.M., Dunbar, R.B., Schrag, D.P., 2000. New views of tropical paleoclimates from corals. *Quaternary Science Reviews* 19, 45-64.

Galbraith, R.F., Roberts, R.G., Laslett, G.M., Yoshida, H., Olley, J.M., 1999. Optical dating of single and multiple grains of quartz from Jinmium Rock Shelter, northern Australia: Part 1, experimental design and statistical models. *Archaeometry* 41, 339-364.

Grant, K.M., Rohling, E.J., Westerhold, T., Zabel, M., Heslop, D., Konijnendijk, T., Lourens, L., 2017. A 3 million year index for North African humidity/aridity and the implication of potential pan-African Humid periods. *Quaternary Science Reviews* 171, 100-118.

Guérin, G., Mercier, N., Adamiec, G., 2011. Dose-rate conversion factors: update. *Ancient TL* 29, 5-8.

Guyard, H., Chapron, E., St-Onge, G., Anselmetti, F.S., Arnaud, F., Magand, O., Francus, P., Mélières, M.-A., 2007. High-altitude varve records of abrupt environmental changes and mining activity over the last 4000 years in the Western French Alps (Lake Bramant, Grandes Rousses Massif). *Quaternary Science Reviews* 26, 2644-2660.

Hahn, A., Kliem, P., Oehlerich, M., Ohlendorf, C., Zolitschka, B., 2014. Elemental composition of the Laguna Potrok Aike sediment sequence reveals paleoclimatic changes over the past 51 ka in southern Patagonia, Argentina. *Journal of Paleolimnology* 52, 349-366.

Harle, K.J., Heijnis, H., Chisari, R., Kershaw, A.P., Zoppi, U., Jacobsen, G., 2002. A chronology for the long pollen record from Lake Wangoom, western Victoria (Australia) as derived from uranium/thorium disequilibrium dating. *Journal of Quaternary Science* 17, 707-720.

Harrison, S.P., Bartlein, P., 2012. Records from the Past, Lessons for the Future: What the Palaeorecord Implies about Mechanisms of Global Change, in: Henderson-Sellers, A., McGuffie, K. (Eds.), *The Future of the World's Climate*. Elsevier Science, pp. 403-436.

Heiri, O., Lotter, A., Lemcke, G., 2001. Loss on ignition as a method for estimating organic and carbonate content in sediments: reproducibility and comparability of results. *Journal of Paleolimnology* 25, 101-110.

Hesse, P.P., McTainsh, G.H., 2003. Australian dust deposits: modern processes and the Quaternary record. *Quaternary Science Reviews* 22, 2007-2035.

Hofmann, H., Newborn, D., Cartwright, I., Cendón, D.I., Raiber, M., 2019. Groundwater mean residence time of a sub-tropical barrier sand island. *Hydrology and Earth System Science Discussions* 1-32.

Hogg, A.G., Hua, Q., Blackwell, P.G., Niu, M., Buck, C.E., Heaton, T.J., Guilderson, T.P., Zimmerman, S.R.H., Palmer, J.G., Turney, C.S.M., Reimer, P.J., Reimer, R.W., 2013. Shcal13 Southern Hemisphere calibration, 0-50,000 years cal BP. *Radiocarbon* 55, 1889-1903.

Ihaka, R., Gentleman, R., 2016. R statistical computing program, 3.3.1 ed. The R Foundation for Statistical Computing.

Jacobs, Z., Duller, G.A.T., Wintle, A.G., 2006. Interpretation of single grain  $D_e$  distributions and calculation of  $D_e$ . *Radiation Measurements* 41, 264-277.

Jouve, G., Francus, P., Lamoureux, S., Provencher-Nolet, L., Hahn, A., Haberzettl, T., Fortin, D., Nuttin, L., 2013. Microsedimentological characterization using image analysis and  $\mu$ -XRF as indicators of sedimentary processes and climate changes during Lateglacial at Laguna Potrok Aike, Santa Cruz, Argentina. *Quaternary Science Reviews* 71, 191-204.

Kawagata, S., 2001. Tasman Front shifts and associated paleoceanographic changes during the last 250,000 years: foraminiferal evidence from the Lord Howe Rise. *Marine Micropaleontology* 41, 167-191.

Kemp, C.W., Tibby, J., Arnold, L.J., Barr, C., 2019. Australian hydroclimate during Marine Isotope Stage 3: A synthesis and review. *Quaternary Science Reviews* 204, 94-104.

- Kershaw, P., Moss, P., Van Der Kaars, S., 2003. Causes and consequences of long-term climatic variability on the Australian continent. *Freshwater Biology* 48, 1274-1283.
- Kershaw, A.P., Bretherton, S.C., van der Kaars, S., 2007a. A complete pollen record of the last 230 ka from Lynch's Crater, north-eastern Australia. *Palaeogeography, Palaeoclimatology, Palaeoecology* 251, 23-45.
- Kershaw, A.P., McKenzie, G.M., Porch, N., Roberts, R.G., Brown, J., Heijnis, H., Orr, M.L., Jacobsen, G., Newall, P.R., 2007b. A high-resolution record of vegetation and climate through the last glacial cycles from Caledonia Fen, southeastern highlands of Australia. *Journal of Quaternary Science* 22, 481-500.
- Kienel, U., Kirillin, G., Brademann, B., Plessen, B., Lampe, R., Brauer, A., 2017. Effects of spring warming and mixing duration on diatom deposition in deep Tiefer See, NE Germany. *Journal of Paleolimnology* 57, 37-49.
- Killick, R., Eckley, I.A., 2014. Changepoint: An R Package for Changepoint Analysis. *Journal of Statistical Software*; Vol 1, Issue 3 (2014).
- Köhler, P., Nehrbass-Ahles, C., Schmitt, J., Stocker, T.F., Fischer, H., 2017. Continuous record of the atmospheric greenhouse gas carbon dioxide (CO<sub>2</sub>), raw data, In supplement to: Köhler, P et al. (2017): A 156 kyr smoothed history of the atmospheric greenhouse gases CO<sub>2</sub>, CH<sub>4</sub>, and N<sub>2</sub>O and their radiative forcing. *Earth System Science Data*, 9(1), 363-387, <https://doi.org/10.5194/essd-9-363-2017>. PANGAEA.
- Kylander, M.E., Ampe, L., Wohlfarth, B., Veres, D., 2011. High-resolution X-ray fluorescence core scanning analysis of Les Echets (France) sedimentary sequence: new insights from chemical proxies. *Journal of Quaternary Science* 26, 109-117.
- Lamy, F., Gersonde, R., Winckler, G., Esper, O., Jaeschke, A., Kuhn, G., Ullermann, J., Martinez-Garcia, A., Lambert, F., Kilian, R., 2014. Increased dust deposition in the Pacific Southern Ocean during glacial periods. *Science* 343, 403-407.
- Leach, L.M., 2011. Hydrology and physical setting of North Stradbroke Island. *Proceedings of the Royal Society of Queensland* 117, 21-46.
- Lisiecki, L.E., Raymo, M.E., 2005. A Pliocene-Pleistocene stack of 57 globally distributed benthic  $\delta^{18}\text{O}$  records. *Paleoceanography* 20.

Lo, L., Chang, S.-P., Wei, K.-Y., Lee, S.-Y., Ou, T.-H., Chen, Y.-C., Chuang, C.-K., Mii, H.-S., Burr, G.S., Chen, M.-T., Tung, Y.-H., Tsai, M.-C., Hodell, D.A., Shen, C.-C., 2017. Nonlinear climatic sensitivity to greenhouse gases over past 4 glacial/interglacial cycles. *Scientific Reports* 7, 4626.

Longmore, M.E., 1997. The mid-Holocene "Dry" Anomaly on the Mid-Eastern Coast of Australia: Calibration of Palaeowater Depth as a Surrogate for Effective Precipitation using Sedimentary Loss on Ignition in the Perched Lake Sediments of Fraser Island, Queensland. *Palaeoclimates* 4:46023.

Löwemark, L., Chen, H.F., Yang, T.N., Kylander, M., Yu, E.F., Hsu, Y.W., Lee, T.Q., Song, S.R., Jarvis, S., 2011. Normalizing XRF-scanner data: a cautionary note on the interpretation of high-resolution records from organic-rich lakes. *Journal of Asian Earth Sciences* 40, 1250–1256.

Lukenbach, M.C., Hokanson, K.J., Moore, P.A., Devito, K.J., Kettridge, N., Thompson, D.K., Wotton, B.M., Petrone, R.M., Waddington, J.M., 2015. Hydrological controls on deep burning in a northern forested peatland. *Hydrological Processes* 29, 4114-4124.

Mackenzie, L., Heijnis, H., Gadd, P., Moss, P., Shulmeister, J., 2017. Geochemical investigation of the South Wellesley Island wetlands: Insight into wetland development during the Holocene in tropical northern Australia. *The Holocene* 27, 566-578.

Maroulis, J.C., Nanson, G.C., Price, D.M., Pietsch, T., 2007. Aeolian–fluvial interaction and climate change: source-bordering dune development over the past ~100 ka on Cooper Creek, central Australia. *Quaternary Science Reviews* 26, 386-404.

Marshall, M.H., Lamb, H.F., Huws, D., Davies, S.J., Bates, R., Bloemendal, J., Boyle, J., Leng, M.J., Umer, M., Bryant, C., 2011. Late Pleistocene and Holocene drought events at Lake Tana, the source of the Blue Nile. *Global and Planetary Change* 78, 147-161.

Martin, L., Mooney, S., Goff, J., 2014. Coastal wetlands reveal a non-synchronous island response to sea-level change and a palaeostorm record from 5.5 kyr to present. *The Holocene* 24, 569-580.

Martinez, J.I., DeDeckker, P., Barrows, T.T., 2002. Palaeoceanography of the western Pacific warm pool during the last glacial maximum: long-term climatic monitoring of the maritime continent., in: Kershaw, P., Bruno, D., Tapper, N., Penny, D., Brown, J. (Eds.), *Bridging Wallace's line*. *Adv GeoEcol*, pp. 147-172.

Mejdahl, V., 1979. Thermoluminescence Dating: Beta-Dose Attenuation in Quartz Grains. *Archaeometry* 21, 61-72.

McGowan, H.A., Petherick, L.M., Kamber, B.S., 2008. Aeolian sedimentation and climate variability during the late Quaternary in southeast Queensland, Australia. *Palaeogeography, Palaeoclimatology, Palaeoecology* 265, 171-181.

Miller, G.H., Fogel, M.L., Magee, J.W., Gagan, M.K., 2016. Disentangling the impacts of climate and human colonization on the flora and fauna of the Australian arid zone over the past 100 ka using stable isotopes in avian eggshell. *Quaternary Science Reviews* 151, 27-57.

Moss, P.T., Kershaw, A.P., 2007. A late Quaternary marine palynological record (oxygen isotope stages 1 to 7) for the humid tropics of northeastern Australia based on ODP Site 820. *Palaeogeography, Palaeoclimatology, Palaeoecology* 251, 4-22.

Moss, P.T., Tibby, J., Petherick, L., McGowan, H., Barr, C., 2013. Late Quaternary vegetation history of North Stradbroke Island, Queensland, eastern Australia. *Quaternary Science Reviews* 74, 257-272.

Nanson, G.C., Price, D.M., Jones, B.G., Maroulis, J.C., Coleman, M., Bowman, H., Cohen, T.J., Pietsch, T.J., Larsen, J.R., 2008. Alluvial evidence for major climate and flow regime changes during the middle and late Quaternary in eastern central Australia. *Geomorphology* 101, 109-129.

Neal, R., Stock, E., 1986. Pleistocene occupation in the south-east Queensland coastal region. *Nature* 323, 618-621.

Nilsson, M., Klarqvist, M., Bohlin, E., Possnert, G., 2001. Variation in  $^{14}\text{C}$  age of macrofossils and different fractions of minute peat samples dated by AMS. *The Holocene* 11, 579–586.

Oksanen, J., Blanchet, F.G., Friendly, M., Kindt, R., Legendre, P., McGlinn, D., Minchin, P.R., R. B. O'Hara, Simpson, G.L., Solymos, P., Stevens, M.H.H., Szoecs, E., Wagner, H., 2018. *Community Ecology Package*, 2.5-2 ed, pp. Ordination methods, diversity analysis and other functions for community and vegetation ecologists.

Parrenin, F., Masson-Delmotte, V., Köhler, P., Raynaud, D., Paillard, D., Schwander, J., Barbante, C., Landais, A., Wegner, A., Jouzel, J., 2013. Antarctic Temperature Stack (ATS) from five different ice cores (EDC, Vostok, Dome Fuji, TALDICE, and EDML), In supplement to: Parrenin, F et al. (2013): Synchronous change of atmospheric  $\text{CO}_2$  and Antarctic temperature during the last deglacial warming. *Science*, 339 (6123), 1060-1063, <https://doi.org/10.1126/science.1226368>. PANGAEA.

Patton, N.R., Ellerton, D., Shulmeister, J., 2019. High resolution remapping of the coastal dune fields of south east Queensland, Australia: a morphometric approach. *Journal of Maps* 15, 578-589.

- Pelejero, C., Calvo, E., Barrows, T.T., Logan, G.A., De Deckker, P., 2006. South Tasman Sea alkenone palaeothermometry over the last four glacial/interglacial cycles. *Marine Geology* 230, 73-86.
- Petherick, L., Bostock, H., Cohen, T.J., Fitzsimmons, K., Tibby, J., Fletcher, M.-S., Moss, P., Reeves, J., Mooney, S., Barrows, T., Kemp, J., Jansen, J., Nanson, G., Dosseto, A., 2013. Climatic records over the past 30 ka from temperate Australia – a synthesis from the Oz-INTIMATE workgroup. *Quaternary Science Reviews* 74, 58-77.
- Petherick, L., McGowan, H., Moss, P., 2008. Climate variability during the Last Glacial Maximum in eastern Australia: evidence of two stadials? *Journal of Quaternary Science Review* 23, 787-802.
- Petherick, L.M., McGowan, H.A., Kamber, B.S., 2009. Reconstructing transport pathways for late Quaternary dust from eastern Australia using the composition of trace elements of long travelled dusts. *Geomorphology* 105, 67-79.
- Petherick, L.M., Moss, P.T., McGowan, H.A., 2017. An extended Last Glacial Maximum in subtropical Australia. *Quaternary International* 432, 1-12.
- Pleskot, K., Tjallingii, R., Makohonienko, M., Nowaczyk, N., Szczuciński, W., 2018. Holocene paleohydrological reconstruction of Lake Strzeszyńskie (western Poland) and its implications for the central European climatic transition zone. *Journal of Paleolimnology* 59, 443-459.
- Prescott, J.R., Hutton, J.T., 1994. Cosmic ray contributions to dose rates for luminescence and ESR dating: Large depths and long-term time variations. *Radiation Measurements* 23, 497-500.
- Profe, J., Neumann, L., Novothny, Á., Barta, G., Rolf, C., Frechen, M., Ohlendorf, C., Zolitschka, B., 2018. Paleoenvironmental conditions and sedimentation dynamics in Central Europe inferred from geochemical data of the loess-paleosol sequence at Süttő (Hungary). *Quaternary Science Reviews* 196, 21-37.
- Rees, A.B.H., Cwynar, L.C., Fletcher, M.-S., 2015. Southern Westerly Winds submit to the ENSO regime: A multiproxy paleohydrology record from Lake Dobson, Tasmania. *Quaternary Science Reviews* 126, 254-263.
- Rees-Jones, J., 1995. Optical dating of young sediments using fine-grain quartz. *Ancient TL* 13, 914.
- Rees-Jones, J., Tite, M.S., 1997. Optical dating results for British archaeological sediments. *Archaeometry* 36, 177-187.

Reeves, J.M., Barrows, T.T., Cohen, T.J., Kiem, A.S., Bostock, H.C., Fitzsimmons, K.E., Jansen, J.D., Kemp, J., Krause, C., Petherick, L., Phipps, S.J., Members, O.-I., 2013. Climate variability over the last 35,000 years recorded in marine and terrestrial archives in the Australian region: an OZ-INTIMATE compilation. *Quaternary Science Reviews* 74, 21-34.

Roberts, H.M., Bryant, C.L., Huws, D.G., Lamb, H.F., 2018. Generating long chronologies for lacustrine sediments using luminescence dating: a 250,000 year record from Lake Tana, Ethiopia. *Quaternary Science Reviews* 202, 66-77.

Rohling, E.J., Grant, K., Bolshaw, M., Roberts, A.P., Siddall, M., Hemleben, C., Kucera, M., 2009. Antarctic temperature and global sea level closely coupled over the past five glacial cycles. *Nature Geoscience* 2, 500.

Sáez, A., Valero-Garcés, B.L., Giralt, S., Moreno, A., Bao, R., Pueyo, J.J., Hernández, A., Casas, D., 2009. Glacial to Holocene climate changes in the SE Pacific. The Raraku Lake sedimentary record (Easter Island, 27°S). *Quaternary Science Reviews* 28, 2743-2759.

Smith, S.M., Newman, S., Garrett, P.B., Leeds, J.A., 2001. Differential Effects of Surface and Peat Fire on Soil Constituents in a Degraded Wetland of the Northern Florida Everglades. *Journal of Environmental Quality* 30, 1998-2005.

Stephens, T., Augustinus, P., Rip, B., Gadd, P., Zawadski, A., 2018. Managing land-use effects on Northland dune lakes: lessons from the past. *New Zealand Journal of Marine and Freshwater Research*, 1-21.

Striberger, J., Björck, S., Ingólfsson, Ó., Kjær, K.H., Snowball, I.A.N., Uvo, C.B., 2010. Climate variability and glacial processes in eastern Iceland during the past 700 years based on varved lake sediments. *Boreas* 40, 28-45.

Tachikawa, K., Timmermann, A., Vidal, L., Sonzogni, C., Timm, O.E., 2014. CO<sub>2</sub> radiative forcing and Intertropical Convergence Zone influences on western Pacific warm pool climate over the past 400 ka. *Quaternary Science Reviews* 86, 24-34.

Team-RStudio, 2015. RStudio: Integrated Development for R. RStudio, Inc, Boston, MA.

Tibby, J., Barr, C., Marshall, J.C., Mcgregor, G.B., Moss, P.T., Arnold, L.J., Page, T.J., Questiaux, D., Olley, J., Kemp, J., Spooner, N., Petherick, L., Penny, D., Mooney, S., Moss, E., 2017. Persistence of

wetlands on North Stradbroke Island (south-east Queensland, Australia) during the last glacial cycle: implications for Quaternary science and biogeography. *Journal of Quaternary Science* 32, 770-781.

Turetsky, M.R., Manning, S.W., Wieder, R.K., 2004. Dating recent peat deposits. *Wetlands* 24, 324-356.

Turner, J.N., Holmes, N., Davis, S.R., Leng, M.J., Langdon, C., Scaife, R.G., 2015. A multiproxy (micro-XRF, pollen, chironomid and stable isotope) lake sediment record for the Lateglacial to Holocene transition from Thomastown Bog, Ireland. *Journal of Quaternary Science* 30, 514-528.

Turner, T.E., Swindles, G., Roucoux, K., 2014. Late Holocene ecohydrological and carbon dynamics of a UK raised bog: impact of human activity and climate change. *Quaternary Science Reviews* 84, 65-85.

Turney, C.S.M., Jones, R.T., 2010. Does the Agulhas Current amplify global temperatures during super-interglacials? *Journal of Quaternary Science* 25, 839-843.

Unkel, I., Fernandez, M., Björck, S., Ljung, K., Wohlfarth, B., 2010. Records of environmental changes during the Holocene from Isla de los Estados (54.4°S), southeastern Tierra del Fuego. *Global Planet Change* 74, 99–113.

Van der Bilt, W.G.M., Bakke, J., Vasskog, K., D'Andrea, W.J., Bradley, R.S., Ólafsdóttir, S., 2015. Reconstruction of glacier variability from lake sediments reveals dynamic Holocene climate in Svalbard. *Quaternary Science Reviews* 126, 201-218.

Van der Kaars, S., Miller, G.H., Turney, C.S.M., Cook, E.J., Nürnberg, D., Schönfeld, J., Kershaw, A.P., Lehman, S.J., 2017. Humans rather than climate the primary cause of Pleistocene megafaunal extinction in Australia. *Nature Communications* 8, 1-7.

Vegas-Vilarrúbia, T., Corella, J.P., Pérez-Zanón, N., Buchaca, T., Trapote, M.C., López, P., Sigró, J., Rull, V., 2018. Historical shifts in oxygenation regime as recorded in the laminated sediments of lake Montcortès (Central Pyrenees) support hypoxia as a continental-scale phenomenon. *Science of The Total Environment* 612, 1577-1592.

Walker, J., Lees, B., Olley, J., Thompson, C., 2018. Dating the Cooloola coastal dunes of South-Eastern Queensland, Australia. *Marine Geology* 398, 73-85.

Weltje, G.J., Bloemsmas, M.R., Tjallingii, R., Heslop, D., Röhl, U., Croudace, I.W., 2015. Prediction of Geochemical Composition from XRF Core Scanner Data: A New Multivariate Approach Including Automatic Selection of Calibration Samples and Quantification of Uncertainties, in: Croudace, I.W., Rothwell, R.G. (Eds.), *Micro-XRF Studies of Sediment Cores: Applications of a non-destructive tool for the environmental sciences*. Springer Netherlands, Dordrecht, pp. 507-534.

Weltje, G.J., Tjallingii, R., 2008. Calibration of XRF core scanners for quantitative geochemical logging of sediment cores: Theory and application. *Earth and Planetary Science Letters* 274, 423-438.

Woltering, M., Atahan, P., Grice, K., Heijnis, H., Taffs, K., Dodson, J., 2014. Glacial and Holocene terrestrial temperature variability in subtropical east Australia: branched GDGT distributions in a sediment core from Lake McKenzie. *Quaternary Research* 82, 132–145.

Woodward, C.A., Slee, A., Gadd, P., Zawadzki, A., Hamze, H., Parmar, A., Zahra, D., 2018. The role of earthquakes and climate in the formation of diamictic sediments in a New Zealand mountain lake. *Quaternary International* 470, 130-147.

Woodward, C.A., Gadd, P.S., 2019. The potential power and pitfalls of using the X-ray fluorescence molybdenum incoherent:coherent scattering ratio as a proxy for sediment organic content. *Quaternary International* 514, 30-43.

Wright, H.E.J., 1967. A square-rod piston sampler for lake sediments. *The Journal of Sedimentary Petrology* 37, 975–976.

Zhang, S., Li, T., Chang, F., Yu, Z., Xiong, Z., Wang, H., 2017. Correspondence between the ENSO-like state and glacial-interglacial condition during the past 360 kyr. *Chinese Journal of Oceanology and Limnology* 35, 1018-1031.